THERMAL DIFFUSION TOMOGRAPHY FOR QUANTITATIVE NON-DESTRUCTIVE CHARACTERIZATION OF ELECTRONIC PACKAGES

by

Bahar Öner

B.S., Mechanical Engineering, Middle East Technical University, 2013

Submitted to the Institute for Graduate Studies in
Science and Engineering in partial fulfillment of
the requirements for the degree of
Master of Science

Graduate Program in Mechanical Engineering
Boğaziçi University
2016

ACKNOWLEDGEMENTS

I would like to thank my thesis supervisor Assoc. Prof. Hakan Ertürk for his guidance and support throughout this study. His guidance helped me construct a scientific point of view. I am grateful to him for helping me realize and improve my critical thinking skills. It was a pleasure to discuss and brainstorm with him about this research. I am very glad that we did work together.

I am thankful to my committee members Assist. Prof. İlke Ercan and Assist. Prof. Jeremy K. Mason for their time, warming attitude and constructive critics. I must say that I have always been impressed by curiosity of research and communicational skills of Assist. Prof. Jeremy K. Mason. It was very motivating. At this point, I also would like to thank Assoc. Prof. Derek Baker from Middle East Technical University, who introduced me to the research world when I was a senior undergraduate student. He is the person who inspired me to pursue graduate studies.

I am grateful to my lab mates Refet Ali Yalçın for his technical support and friendship during this study and Beybin İlhan for being an amazing and incredibly supportive friend. I would like to thank my lab mate Ozan Burak Eriçok for the fruitful discussions and exchange of ideas about inverse problems, which I enjoyed all the time. I am also thankful to my colleague Umut Soysal for his friendship and help while writing this thesis.

Finally, I would like to thank my dear mum, wise dad and sweet sister for their continuous love, support, sense of humor and being the most precious part of my life. I am very lucky that I have them in my life.

ABSTRACT

THERMAL DIFFUSION TOMOGRAPHY FOR QUANTITATIVE NON-DESTRUCTIVE CHARACTERIZATION OF ELECTRONIC PACKAGES

Increasing number of transistors and reduction in product size leads to thermal management problems in electronic packages. Thermal interface materials (TIMs) are used as a passive means of thermal management and for high density interconnect packages, TIM helps heat dissipation by reducing thermal contact resistance between chip and integrated heat spreader (IHS). Therefore, TIM quality is critical for effective removal of heat generated by the chip from the package. Identification of defects within TIM is required during package assembly process development so that acceptable TIM quality can be achieved for a reliable thermal performance. While this is possible by qualitative techniques such as X-ray tomography or CSAM, quantitative non-destructive detection based on thermal tomography is proposed as an alternative. High density interconnect flip chip package that includes spreading effect due to different sized IHS and die that is used for CPU of desktop computers and servers is considered in this study. Defect size and location are detected analyzing the measured thermal response of electronic package by solving the resulting inverse problem. Levenberg-Marquardt algorithm is used as an image reconstruction technique as inverse problems are ill-posed in nature and regularization of the system is necessary. The study investigates the feasibility of the method through numerical experiments. Therefore, the experimental data is replaced with synthetic measurement data based on applying random measurement error to simulated measurement data. Results show that thermal tomography has a potential for identification of TIM defects, which cause a measurable effect regarding package specifications.

ÖZET

ELEKTRONİK PAKETLERİN NİCELİKSEL TAHRİBATSIZ MUAYENESİ İÇİN ISIL DİFÜZYON GÖRÜNTÜLEME

Artan transistor sayısı ve ürün boyutunun küçülmesi elektronik paketlerde ısıl yönetim sorunlarına sebep olmaktadır. Isıl arayüz malzemeleri, yüksek yoğunluklu bağlantılı paketlerde pasif ısıl yönetimini sağlamak amacıyla kullanılmaktadır. Isıl ara yüz malzemeleri, çip ile birleştirilmiş ısı dağıtıcı arasındaki ısıl temas direncini azaltarak ısı kaybına yardımcı olur. Bu nedenle, çip tarafından üretilen ısının paketten etkili bir şekilde uzaklaştırılması için ısıl arayüz malzemesinin kalitesi son derece önemlidir. Güvenilir bir ısıl performansı sağlayacak, kabul edilebilir kalitede bir ısıl arayüz malzemesi elde edebilmek için paket montaj süreci geliştirilmesinde ısıl arayüz malzemesindeki kusurların tespit edilmesi gerekir. Bu amaçla X-ray görüntüleme veya bilgisayar destekli tarama ses mikroskobu gibi niteliksel yöntemler kullanılabildiği gibi, ısıl görüntüleme tabanlı niceliksel tahribatsız muayene de bir alternatif olarak sunulmaktadır. Bu çalışmada, masaüstü bilgisayarların ve sunucuların işlemcilerinde kullanılan ve birleştirilmiş ısı dağıtıcı ve çipin farklı boyutlarda olmasından kaynaklanan yayılma etkisini gösteren yüksek yoğunluklu bağlantılı ters yüz edilmiş çipler değerlendirilmiştir. Elektronik paketin ısıl tepkisinin ölçümü neticesinde oluşan ters problemi çözerek, kusur büyüklüğü ve yeri tespit edilmiştir. Ters problemler doğası gereği kötü konumlanmış olduğundan ve bu nedenle sistemin düzenlileştirilmesi gerektiğinden, görüntü yeniden yapılandırma tekniği olarak Levenberg-Marquardt algoritması kullanıldı. Bu çalışmada nümerik deneyler kullanılarak, önerilen metodun uygulanabilirliği incelenmiştir. Bu nedenle, deneysel veri, simüle edilmiş ölçüm verisine rassal ölçüm hatası ekleyerek elde edilen sentetik ölçüm verisiyle değiştirilmiştir. Sonuçlar, ısıl görüntüleme yönteminin, paket spesifikasyonlarına göre ölçülebilecek bir etkiye sebep olabilecek ısıl arayüz malzemesi kusurlarını tespit etme potansiyeli olduğunu göstermektedir.

TABLE OF CONTENTS

ACKNOWLEDGEMENTS iii

ABSTRACT iv

ÖZET v

LIST OF FIGURES viii

LIST OF TABLES xi

LIST OF SYMBOLS xii

LIST OF ACRONYMS / ABBREVIATIONS xiv

1. INTRODUCTION 1

1.1. Problem Overview 1

1.2. Literature Survey 3

2. PROBLEM STATEMENT AND FORMULATION 16

2.1. Problem Statement 16

2.2. Direct Problem Formulation 19

2.3. Inverse Problem Formulation 22

2.4. Levenberg-Marquardt Algorithm (LMA) 24

2.5. Stopping Criteria 28

3. GRID INDEPENDENCY AND MODEL VERIFICATION 31

3.1. Grid Independency Study 31

3.2. Verification Study 35

4. RESULTS AND DISCUSSION 36

4.1. Simulated Measurements 36

4.2. Void Fraction Estimations 42

5. CONCLUSION AND FUTURE WORK 54

REFERENCES 57

LIST OF FIGURES

Figure 1.1. Simplified schematic of electronic packaging represented in [15] 4

Figure 1.2. (a) Flip chip technology with one TIM for mobile applications
(b) Flip chip technology with a second TIM for higher power applications
(Adapted from [16]) 5

Figure 1.3. Schematic representation of the origin of contact resistance and TIM use
(not to scale) [17] 5

Figure 1.4. CSAM working principle [21] 7

Figure 1.5. X-ray analysis schematic 8

Figure 1.6. Schematic of Liquid Crystal Thermography arrangement [25] 9

Figure 2.1. Electronic package used in thermal performance test (Test-1) 16

Figure 2.2. Electronic package used in thermal tomography (Test-2) 17

Figure 2.3. Simplified version of electronic package model used in thermal performance
test simulations 18

Figure 2.4. Simplified version of electronic package model used in thermal tomography
simulation (dimensions not to scale) 18

Figure 2.5. Levenberg-Marquardt algorithm (Adapted from [34]) 25

Figure 2.6. L-curve form for discrete inverse problems (Adapted from [59]) 27

Figure 2.7. Probability density function of the normal distribution 29

Figure 3.1. Temperature variation at die base surface (*z*=0 mm) along x axis, *y*=5 mm for
thermal performance test (Test-1) 32

Figure 3.2. Temperature distribution at die bottom surface (z=0 mm) at t=100ms along
x axis, y=5 mm for thermal tomography (Test-2)..... 33

Figure 3.3. Temperature distribution at IHS top surface (z=2.34 mm) at t=100 ms along
x axis, y=15 mm for thermal tomography (Test-2) 34

Figure 3.4. Temperature variation at die bottom surface (z=0 mm) along x axis, y=5 mm
for Icepak [62] and COMSOL models for thermal performance test 35

Figure 4.1. Void size and location effect on thermal performance test (Test-1) 37

Figure 4.2. Void fraction of TIM1 used in thermal tomography test simulation 38

Figure 4.3. Temperature distribution [K] at die bottom surface in thermal performance
test (Test-1) for (a) ideal case, (b) case shown in Figure 4.2 39

Figure 4.4. Die base temperature distribution [K] from solution of direct problem 40
Figure 4.5. Simulated measurements, IHS temperature distribution [K] with no error estimation for the case in Figure 4.2 41
Figure 4.6. Synthetic measurement data by introducing random error and uncertainty to simulated IHS temperature distribution [K] estimation for the case in Figure 4.2 42
Figure 4.7. Singular value decomposition (SVD) for the case in Figure 4.2 44
Figure 4.8. L-curve for the case represented in Figure 4.2 to decide on regularization parameter 45
Figure 4.9. Ad-hoc filtered void fraction estimation for the case in Figure 4.2 for measurements with no random error 46
Figure 4.10. Ad-hoc filtered void fraction estimation for the case in Figure 4.2 for measurements with uncertainty and random measurement error σ.....47
Figure 4.11. Ad-hoc filtered void fraction estimation for the case in Figure 4.2 for measurements with uncertainty and random measurement error 2σ..... 47
Figure 4.12. Void fraction estimation for parametric study for alteration coefficient for λ at each iteration in LMA for the case in Figure 4.2 with uncertainty and random measurement error σ 48
Figure 4.13. Ad-hoc filtered void fraction estimations for the case in Figure 4.2 for measurements with uncertainty and random measurement error σ to investigate optimum measurement duration 49
Figure 4.14. Ad-hoc filtered void fraction estimations for the case in Figure 4.2 for measurements with uncertainty and random measurement error σ to investigate optimum measurement time interval 50
Figure 4.15. Ad-hoc filtered void fraction estimation for the case in Figure 4.2 for measurements with uncertainty and random measurement error σ using dimensional reduction..... 51
Figure 4.16. Ad-hoc filtered void fraction estimation for the case in Figure 4.2 for measurements with uncertainty and random measurement error σ, using ad-hoc filtering and dimensional reduction at each iteration 52

Figure 4.17. Effect of thermal performance test (Test-1) temperature rise on estimation results for measurements with uncertainty and random measurement error σ 53

LIST OF TABLES

Table 2.1. Component material properties 19
Table 3.1. Mesh details of COMSOL model created for thermal performance test 31
Table 3.2. Mesh details of COMSOL model created for thermal tomography test 33
Table 4.1. Center coordinates and sizes of void fractions presented in Figure 4.2 38

LIST OF SYMBOLS

C	Heat capacity (ρc) [J/m^3-K]
C_N	Condition number
$\mathbf{C_{TIM}}$	Heat capacity (ρc) distribution for TIM1 [J/m^3-K]
$C_{TIM,ideal}$	Heat capacity (ρc) for ideal TIM1 [J/m^3-K]
C_v	Heat capacity (ρc) of void [J/m^3-K]
$F(\varphi)$	Objective function to be minimized
h	Convective heat transfer coefficient [W/m^2-K]
$\mathbf{J}$	Jacobian matrix
k	Thermal conductivity [W/m-K]
$\mathbf{k_{TIM}}$	Thermal conductivity distribution for TIM1 [W/m-K]
$k_{TIM,ideal}$	Thermal conductivity of ideal TIM1 [W/m-K]
k_v	Thermal conductivity of void [W/m-K]
L_x	Size of the package along x-coordinate
$L_{x,die}$	Size of die along x-coordinate
L_y	Size of the package along y-coordinate
$L_{y,die}$	Size of die along y-coordinate
L_z	Thickness of the package (along z-coordinate)
$L_{z,die}$	Thickness of the die
$L_{z,TIM}$	Thickness of die and TIM1
N_s	Number of sensors
N_t	Number of measurements takes at different times
N_u	Number of unknown parameters
q''	Heat flux [W/m^2]
$\mathbf{r}$	Coordinate vector
$\mathbf{R}$	Residual
$\mathbf{S}$	Singular values matrix
$\mathbf{t}$	Time vector
T	Temperature [K]
$\mathbf{T_m}$	Temperatures calculated for a given set of properties at sensor locations at measurement times [K]

T_∞	Ambient temperature [K]
U, V	Orthogonal matrices
V	Volume [m^3]
V_v	Volume of void [m^3]
X	Difference between solution of the void fractions
Y	Temperatures measured by sensors at measurement times [K]
ε	Convergence criteria
λ	Damping coefficient for Levenberg-Marquardt algorithm
$\mathbf{\Omega}$	Conditioning matrix for Levenberg-Marquardt algorithm
σ	Standard deviation of measurement error
σ_{pi}	Uncertainty of the property or the boundary condition p_i
σ_s	Uncertainty due to uncertainties in the properties of electronic package layers and boundary conditions applied
$\boldsymbol{\varphi}$	Void fraction distribution for TIM1
i	i-th sensor
j	j-th time step
m	measurements
n	n-th unknown void fraction
k	k-th iteration
p	property
s	sensor
'	Exact solution of the problem

LIST OF ACRONYMS / ABBREVIATIONS

AFM	Atomic Force Microscope
CSAM	Computerized Scanning Acoustic Microscopy
CGM	Conjugate Gradient Method
FEM	Finite Element Method
IC	Integrated Circuit
IHS	Integrated Heat Spreader
IR	Infrared
FEM	Finite Element Model
LMA	Levenberg-Marquardt Algorithm
MCM	Multichip Module
NDT	Non-Destructive Testing
PCB	Printed Circuit Board
PWB	Printed Wire Board
SAM	Scanning Acoustic Microscope
SSE	Sum of Squares of Errors
SVD	Singular Value Decomposition
TAB	Tape Automated Bonding
TDR	Time Domain Reflectometry
TLC	Thermochromic Liquid Crystals

1. INTRODUCTION

1.1. Problem Overview

Moore foresaw that the number of transistors incorporated in a chip would approximately double every two years [1]. Commitment of industry to follow Moore's law leads to incorporating more transistors in chips. Although more efficient chips are produced in terms of power per performance due to improved manufacturing processes, transistor architecture and chip design, combined with recent trends in mobility and shrinking sizes lead to high power densities that still concern the industry in terms of thermal management. Considering the holistic approach industry have been adapting, thermal management must be addressed in cooling system and package level besides solutions improving transistor architecture, manufacturing processes and chip design.

Electronic package connects the die (chip) to the motherboard in order to achieve a reliable performance in terms of signal and power delivery, heat dissipation and mechanical protection. In order to overcome heat dissipation problem in the package, thermal interface layers (TIMs) are assembled between package layers to reduce thermal contact resistance between these layers. While TIM1 is placed between chip and integrated heat spreader (IHS), TIM2 is placed between the IHS of the package and heat sink. Thus, quality of TIM layers is crucial for desired cooling performance. Thermal greases, phase change materials and thermally conductive elastomers are commercially used thermal interface materials [2].Yet, none of them perform ideally as during assembly process, defects such as dendrite growth, interfacial delaminations, metal migration, voids and micro cracks can be observed in the TIMs due to curing speed or deposition technique or speed [3-4].

The objective of the assembly process development for a new product is to identify the optimal assembly process parameters that would lead to packages with high thermal, mechanical and electrical performance. Therefore, high number of prototype packages, often referred as "test vehicles", are produced and tested to optimize process parameters during the

assembly process development. Thermal test is one of the tests applied to these test vehicles and it quantifies the thermal resistance of the package, which is defined from the highest temperature of the die, also known as junction temperature, to the temperature of top surface of the lid, also known as case temperature. If the measured test vehicle's thermal resistance is beyond the targeted specification, this means the package has a defect and the defect must be identified so that the related process parameter must be improved.

Defects leading to thermal failure such as voids and delamination have direct and similar impact on the system thermal performance and can be treated equally [5]. Identification of defects on TIM1 is more critical than that of TIM2 since same sized defect on TIM1 reduces thermal performance of the system approximately 25 times more than that of TIM2 [5]. In order to optimize assembly process, TIM defects, especially defects on TIM1, can be identified qualitatively using non-destructive imaging techniques such as computerized scanning acoustic microscopy (CSAM), X-ray imaging and liquid crystal thermography. Recently, infrared (IR) imaging has been proposed as a powerful technique for inspection of defects that produce thermal failure modes in TIM [3]. IR imaging measures temperature response of the system to the applied heat flux using an IR camera in order to observe defected region. All these non-invasive testing techniques should be considered as complementary and qualitative. Although qualitative defect detection is a common inspection technique in industrial applications, quantitative defect detection has been a recent interest of researchers.

Thermal tomography is a thermal imaging technique, which can enable both qualitative and quantitative inspection. Earlier research demonstrated the use of thermal tomography in medical [6-7] and materials science [8-9] applications. It was shown that thermal tomography is capable of rapid, full-field and low-cost defect detection [10]. Although thermal diffusion rate can limit defect characterization accuracy, research on quantitative defect detection using thermal tomography is still ongoing.

In electronic packaging, thermal tomography can be performed adapting a similar approach to IR imaging. The specimen can be heated either by applying die power or using an external flash, and then taking temperature data from high speed IR cameras or sensor readings from the target surface. Unknown material properties are estimated by image reconstruction using temperature measurements. Defect is characterized by estimated material properties.

Estimation of material properties using thermal tomography is an ill-posed inverse problem. Inverse problems are prone to problems in regards to existence, uniqueness and stability of the solution. Therefore, thermal tomography problems can be solved using various image reconstruction techniques that are capable of regularizing the system to cope with these problems.

The main difficulties for the application of thermal tomography for defect characterization in an electronic package which is subject to spreading effect due to different sized IHS and die are as follows: (i) As heat diffuses laterally, spreading effect leads to loss of thermal signal, which is used in the solution of resulting inverse problem. (ii) The ill-posed nature of the inverse problem necessitates optimization of system regularization and system specific test procedure.

1.2. Literature Survey

Electronic packaging connects circuit to the application environment in order to achieve a desirable function and protect the circuits. Different levels of electronic packages are illustrated in Figure 1.1. Gate to gate interconnections are made on the silicon die (chip). Then, first level interconnects connects the chip to the package substrate in order to protect the circuits and perform a desirable function. One or more such first level packages are connected to the printed circuit boards (PCBs) or printed wire boards (PWBs) by second level interconnects. Multiple PCBs or PWBs are connected to motherboard providing operation of the complete system including processing, graphics and sound management.

Common chip to substrate connections are wire bonding, tape automated bonding (TAB) and flip chip (bump bonding) [11-12]. Among these, flip chip technology is more advantageous in terms of electrical performance speed, size, input/output connection flexibility, interconnection durability and increased productivity as higher number of bonds can be made at the same time [11, 13-14]. Flip chip technology is growing in today’s semiconductor industry due to its compactness.

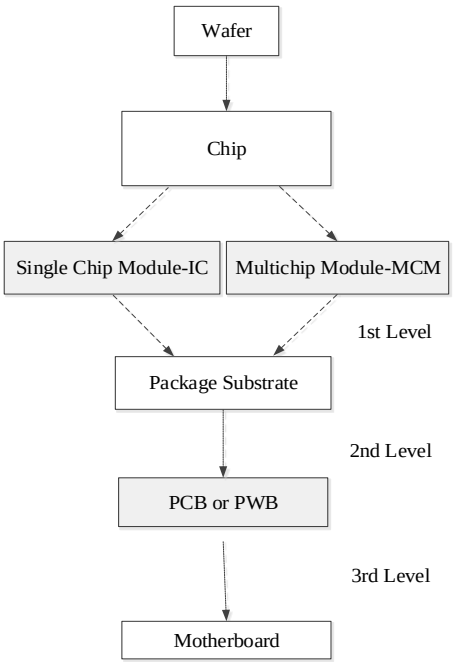

Figure 1.1. Simplified schematic of electronic packaging represented in [15]

Flip chip packaging technology has many application areas and its popularity is attributed to its compactness. Therefore, it is not only preferred for high performance products such as desktop and server central processing units, but also used for mobile devices such as cellular phones, laptops, digital cameras and some medical devices. There are mainly two architectures of flip chip packages. First type includes only one thermal interface material (TIM) placed in between die and a heat spreader or another active cooling system. Second architecture makes use of two TIMs, one placed in between die and integrated heat spreader (IHS) that is referred asTIM1 and the other is sandwiched in between IHS and heat sink that is referred as TIM2. The first architecture is primarily used in laptop applications due to lower rate of heat dissipation while the second one is mainly used for desktops and servers which require higher heat dissipation rates [16]. The first and second types of flip chip packages are schematically represented in Figure 1.2.a and Figure 1.2.b, respectively.

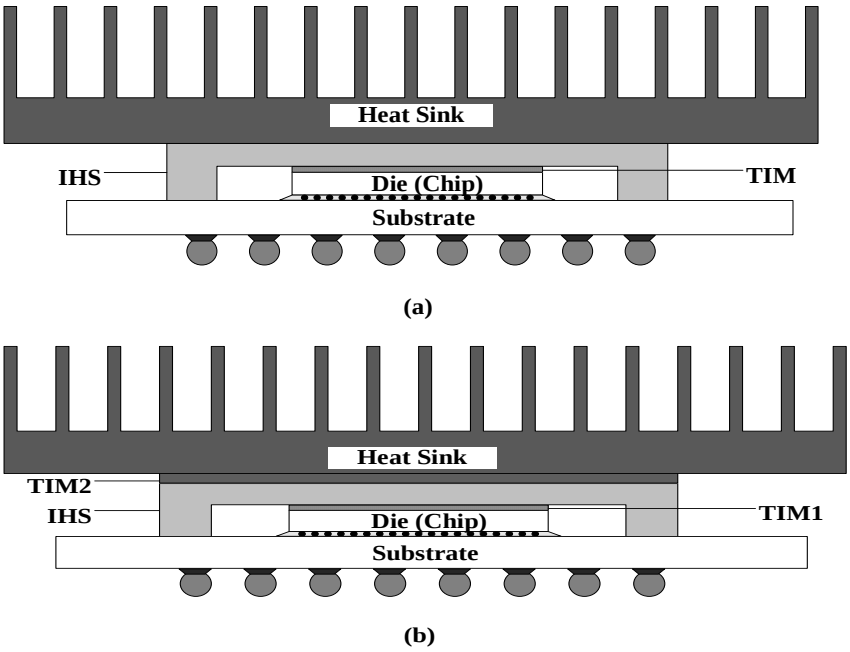

Figure 1.2. (a) Flip chip technology with one TIM for mobile applications

(b) Flip chip technology with a second TIM for higher power applications (Adapted from [16])

When two solid materials are brought in contact, a thermal resistance is observed at the interface leading to a temperature drop. Thermal interface materials are used to reduce thermal contact resistance between package layers to reduce the resulting thermal resistance in the heat transfer path. Although the interface between package layers might look perfect to human eye, microscopic irregularities exist between them in reality. Figure 1.3 is a magnified illustration of thermal interface material filling irregular gaps between the die and integrated heat spreader (IHS).

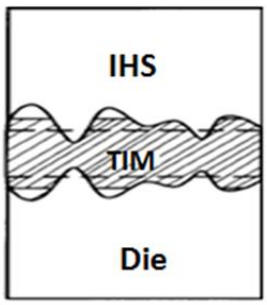

Figure 1.3. Schematic representation of the origin of contact resistance and TIM use (not to scale) [17]

Defects such as voids and delaminations can be observed within thermal interface material that might cause thermal failure. Gektin [5] mentions that 5% of void within TIM1 reduces thermal performance of the system by 70 to 130%, depending on the thermal interface material used. Therefore, identification of voids within TIM is crucial for a reliable thermal performance. Effect of voids and delamination on thermal performance is investigated in [5] using both numerical models and experimental approach. In the study, delamination is defined as defects having up to 1 μm thickness, whereas voids are the defects larger than 1 μm thickness. Although it can be intuitively considered that voids would be a more effective failure mode due to higher volume occupied, effects of both on thermal performance is investigated. The study reveals that the impact of both defects on thermal performance is almost identical. Therefore, delamination can be considered as void in the analysis or vice versa.

A number of non-destructive testing (NDT) techniques are available for defect identification in electronic packages, such as time domain reflectometry (TDR), magnetic microscopy, atomic force microscope (AFM), optical microscope, C-mode scanning acoustic microscopy (CSAM), X-ray, liquid crystal thermography and IR thermometry [3, 18-20]. These techniques have different uses considering defect type, ranging from detection of input/output connectivity and power delivery related failures such as low impedance, high resistance or wire shorting, to mechanical and thermal defects, such as voids and delaminations. Among these, CSAM, X-ray, liquid crystal thermography and IR thermography are commonly used for identification of defects leading to thermal failure modes.

Scanning acoustic microscope (SAM) is a high frequency ultrasonic imaging technique used to investigate defects within optically opaque samples. Ultrasound is a very high frequency sound wave, with wavelengths in the order of μms, that is beyond humans' hearing limit. The underlying mechanism in defect detection using this technique is that ultrasound is not transmitted through air. Figure 1.4 illustrates a CSAM setup. A transducer converts electrical energy into acoustic waves and sends ultrasound to the test sample, which is scanned mechanically. The emitted acoustic waves are transmitted through the coupled liquid (distilled water or alcohol) to the test sample. Here, the coupled liquid enables efficient ultrasound propagation to the solid sample. As the transducer acts as both receiver and emitter, it receives

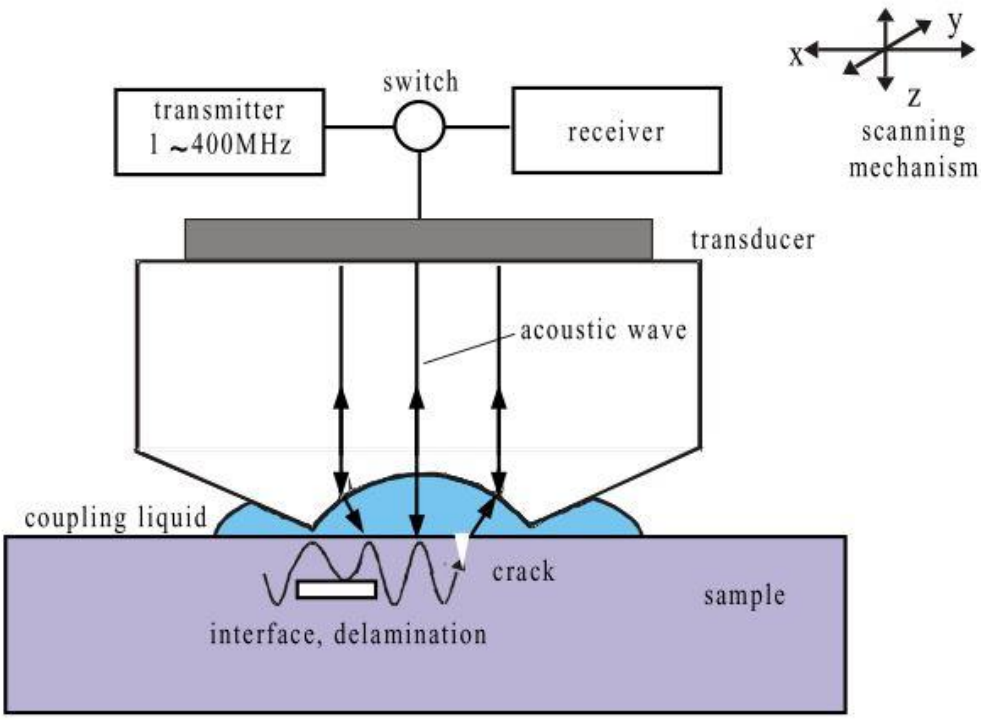

Figure 1.4. CSAM working principle [21]

the reflected wave that is converted into electromagnetic pulses, and these electromagnetic pulses are displayed as pixels. As defects such as delaminations, voids and cracks comprise of air spaces, ultrasound does not pass through these and the defect is identified [21-22].

X-rays are electromagnetic waves with wavelengths in 0.01-10 nm range. X-ray analysis consists of an X-ray source, image detector and a sample holder as represented in Figure 1.5 [23]. A filament in a vacuum tube (X-ray tube) is heated in order to emit electrons. These accelerated electrons pass through a magnetic lens that produces magnetic field, and sent to a tungsten layer. X-ray source is created when electrons suddenly decelerate after hitting the tungsten layer. The sample to be characterized is placed in between X-ray tube and the image detector and X-rays pass through the sample. As density of the sample changes, the energy of X-rays passing through also changes that is captured by image detector, and processes a grayscale image which is visible to human eye. The lower density regions are displayed brighter in the image created, meaning that voids are observed as brighter regions.

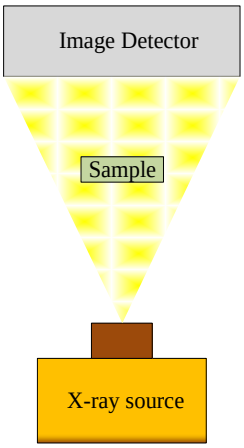

Figure 1.5. X-ray analysis schematic

Liquid crystal thermography makes use of thermochromic liquid crystals (TLC) to observe temperature gradients across the material being inspected [24-25]. Molecular and optical properties of TLCs change with temperature. A stable white light source is used and reflected color of TLC is associated with different temperatures for calibration. The sample under inspection is first coated with a black paint, then after applying TLC, the material is heated. Transparent liquid crystals at low temperature turn into red, yellow, green, blue or violet colors at elevated temperatures as liquid crystals reflect visible light at different wave lengths with changing temperature [25]. Image of the sample is obtained using a digital camera. Figure 1.6 illustrates the schematic of liquid crystal thermography arrangement. As lower temperature areas are considered as regions with lower thermal conductivity, voids entrapped in interface material could be characterized as proposed in [24-25]. Besides, this technique could also be used to identify delaminations and voids entrapped in layers for composite structures [20].

As mentioned earlier, CSAM and X-ray are widely used conventional qualitative nondestructive imaging techniques in electronic packaging [3, 5, 26-27]. While CSAM is superior to X-ray in delamination detection, lateral resolution of CSAM is insufficient to observe interconnect wires and wire breakages unlike X-ray imaging. Although detection of large voids is possible using X-ray, smaller ones are not visible in X-ray results. On the contrary, CSAM detects even small voids due to strong reflection of acoustic waves. Both

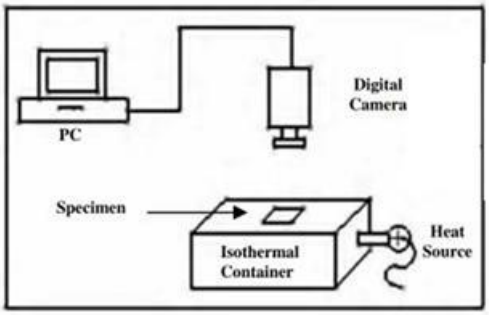

Figure 1.6. Schematic of Liquid Crystal Thermography arrangement [25]

CSAM and X-ray can detect cracks, but only CSAM can give information about crack location and size [28]. As an alternative to these imaging techniques, liquid crystal thermography can be used for defect characterization, especially for characterization of voids and delaminations [24-25]. Although this technique could provide accurate results with fine resolutions at a reasonable cost, it is not convenient when a large number of test vehicles are tested for assembly process development as specimen preparation, i.e. coating and application of liquid crystals, takes some time [24]. More recently, application of infrared (IR) imaging was introduced as qualitative means of defect detection [3, 26]. Radiosity from the test sample in IR wavelengths is collected by an imaging sensor in the camera and converted to electrical signal to be displayed on a screen as emissive power or equivalent temperature values [29]. Pacheco *et al.* [3] and Gupta *et al.* [26] use IR imaging to detect TIM defects qualitatively. They either power up the die or apply external power to monitor the temperature response at the top surface of IHS using an IR camera. The thermal signal disappears after some time due to lateral heat dissipation. In [3], TIM thickness variation is detected after die is powered up.

Gupta *et al.* [26] investigates IR imaging and compares it with CSAM. Using the CSAM and IR images of good, voided and micro-crack introduced units, it was observed that IR imaging was superior to CSAM in detection of micro-cracks while spatial resolution of CSAM was better on void detection. However, the advantage of IR imaging is its direct relation to thermal performance, ease of set up procedure and rapidity of application for large area inspection. Yet, defect image obtained using IR may not be completely visible due to lateral heat dissipation. Considering above-mentioned properties, all these non-invasive testing techniques are suggested as complementary and qualitative.

Thermal tomography provides both qualitative and quantitative inspection, being an alternative to above-mentioned imaging techniques. It was used as a rapid, full-field and low-cost defect detection technique [10]. Unlike other tomography applications such as X-ray, optical, or magnetic resonance, thermal tomography relates system response to the thermal performance. There has been an ongoing research on thermal tomography due to its potential to gather quantitative information related to thermal performance.

Thermal tomography relies on IR thermography data to quantify thermal properties of the material under inspection. In order to identify TIM defects, the test sample can be heated either by applying die power or using an external flash, and then temperature data from high speed IR cameras or sensor readings from the target surface are utilized. Temperature measurements are used in reconstruction of the interface image by estimating the unknown material property distribution so that defect could be characterized.

Tomography problems can be classified as ill-posed inverse problems. In a direct or forward problem, the unknown effect of a known cause is identified. Considering the analysis of thermally conducting system, the temperature distribution is predicted for a given geometry, material properties, initial and boundary conditions through the solution of heat conduction equation. However, the unknown cause of an observed effect is sought after in an inverse problem. For a conducting system, considering the measured temperature response, the inverse problem is either comprised of identification of the unknown system under known boundary conditions, or identification of the unknown boundary conditions for a known system. Solving an inverse problem can be a challenging task as they are usually ill-posed. In 1902, a French mathematician Jacques Hadamard [30] defined well-posedness of a problem based on three criteria:

1. A solution must exist.
2. The solution must be unique.
3. The solution must be stable.

If the problem does not satisfy one or more of the above mentioned criteria, then it can be classified as ill-posed. As Soemers [31] and Colaço *et al.* [32] mention, physics of the event can give insight into fulfillment of 1st criterion, which is the existence of a solution to an

inverse problem. In order to highlight the importance of understanding physical meaning of the problem, Au [33] considers the solution of an inverse problem where the final state is defined at “minimal entropy”. As entropy is continuously generated with time, the solution of such a problem does not exist because going backwards to a stage where entropy is smaller than “minimal entropy” is not possible. A similar approach can be adapted for specific inverse problems in order to decide on existence of a solution. In some cases, the solution to an inverse problem may not be unique, which is stated as 2nd criterion by Hadamard. Considering an inverse heat conduction problem, initial condition estimation for a system that reached steady state might not be unique as the effect of initial condition disappears with time, i.e. different initial conditions might satisfy the same final state [33]. Hadamard’s 3rd criterion implies that small changes in the input data lead to huge changes in the final solution if the problem is ill-posed, which is frequently encountered in experimental studies. Mostly, the stability criterion constitutes a challenge for property estimation problems. In order to cope with problems that inverse problems are prone to in regards to existence, uniqueness and stability of the solution, various regularization or statistical methods are proposed.

Inverse heat transfer problems can be categorized as inverse conduction problem, inverse convection problem, inverse radiation problem or a combination of these, considering the heat transfer mechanisms taking place. Depending on the estimation to be sought for, another classification for inverse heat transfer problems can be as follows:

1. Inverse initial condition estimation problem
2. Inverse boundary condition estimation problem
3. Inverse source estimation problem
4. Inverse geometry estimation problem
5. Inverse property estimation problem

For the extended review of classification of inverse heat transfer problems, interested reader is referred to [34-36]. In thermal tomography problem presented here, conduction takes place as the primary heat transfer mechanism. Therefore, in this study, resulting inverse heat conduction problem is considered in order to estimate material thermal properties. Thus, following discussion is mainly based on inverse conduction problems where material properties are estimated.

Various regularization or statistical methods are proposed for the solution of ill-posed inverse heat transfer problems. Özışık and Orlande [34] propose Levenberg-Marquardt method and conjugate gradient method for parameter estimation, and conjugate gradient method with adjoint problem for both parameter and function estimation for the solution of inverse heat conduction problems. All these methods are iterative techniques based on least squares minimization for solution of nonlinear least squares problem and they have different advantages and disadvantages depending on the application. While Levenberg-Marquardt method converges to Newton-Gauss method in the neighborhood of the ordinary least squares norm, it resembles steepest descent method when subjected to higher regularization. On the other hand, conjugate gradient method seeks the optimal solution iteratively, relying on conjugate directions of descent. The estimation of Jacobian that is comprised of sensitivity coefficients is required for both methods, which is usually computationally expensive. Conjugate gradient method with adjoint problem is proposed to eliminate calculation of Jacobian for the direction of decent. When number of unknown parameters is sufficiently small, Levenberg-Marquardt algorithm or conjugate gradient method appear to be advantageous considering computational cost and their simplicity. Sawaf and Özışık [37] applied Levenberg-Marquardt algorithm to estimate linearly temperature dependent thermal properties of an orthotropic solid using three sensors for temperature measurements where the problem is simplified as a single layer, rectangular geometry. The results show that increasing standard deviation for temperature measurement error leads to increase in estimation errors, as expected. Effect of sensor location on estimations is also investigated in [37]. It was concluded that sensor location does not have a significant effect on estimation accuracy for the problem defined.

Jones *et al.* [38] solves a thermal tomography problem in order to obtain thermal conductivity map of a 2-D plate including a single void. The inverse problem is solved using both genetic algorithm and quasi-Newton's method, with two regularization methods such as truncated singular value and Tikhonov regularization. Genetic algorithm is based on survival of the fittest principle and the most important factor using it is choosing the fitness function that is discussed in detail in [38]. After solving the inverse problem on a larger domain, "zooming" is applied in order to obtain more accurate estimations. They apply so-called "zooming method" by grouping finite elements into larger blocks and obtaining an initial estimate based on these large blocks. After initial estimation, number of blocks is increased at the regions where in-

homogeneity is observed. The inverse problem is resolved by assuming initial conductivity distribution at the inhomogeneous region less than that of the bulk conductivity. It was shown that zooming method provides a higher resolution mapping. Results indicate that Tikhonov and truncated singular value regularizations provide similar solutions while truncated singular value regularization converges faster. However, genetic algorithm provides the most accurate estimations but it is very computationally intensive, necessitating 2000 iterations to solve a 2D problem. Moreover, fitness function selection is important to represent system behavior accurately. While the trade-offs between three methods are carefully investigated, random noise and multiple voided case are not considered in [38].

Conjugate gradient method (CGM) is used for temperature dependent or space and time dependent thermal property estimation in [39-40]. Huang *et al.* [39] solves a one dimensional (1-D) problem in order to estimate temperature dependent thermal properties using CGM. Time and space dependent thermal conductivity of a two dimensional (2-D) system is estimated using CGM in [40], where temperature measurements are obtained from an infrared scanner. The results show that CGM successfully estimates thermal properties of 1-D and 2-D problems.

Modified Newton-Raphson method is used to estimate temperature dependent thermal conductivity and heat capacity of a slab concurrently using two sensors for temperature measurements at the boundaries, where thermal properties are assumed in functional forms in [41]. The results indicate that modified Newton-Raphson method is successful at estimating temperature dependent thermal properties using only two sensors placed at the boundaries, where heat flux is applied. However, the limitation in this study is that a function form is required to represent thermal properties.

Iterative perturbation method, Levenberg-Marquardt and Regularized Newton-Gauss algorithms are compared for quantification of defects within TIM using thermal tomography in [4]. The study shows that all three algorithms can estimate thermal properties of TIM. It was concluded that if the number of measurement data is sufficiently large, prediction accuracy, convergence rate and computational effort are similar for all three algorithms. The study considers a relatively simpler geometry, where spreading effect is not taken into consideration. With spreading introduced, the problem is expected to become more challenging as spreading lead to loss of thermal signal that eventually will obscure property estimation.

Thermal resistance distribution of a die-attach material is estimated in [42]. The problem is formulated as a steady state inverse heat conduction problem. Temperature measurements at the bottom surface of the die are obtained using IR thermography and thermal resistance distribution in the interface is estimated solving the resulting inverse problem using conjugate gradient method. A sensitivity study is performed by comparing different configurations of heat source. The study concludes that streamer shape heat source is the most suitable configuration in order to estimate thermal resistance of interface material using conjugate gradient method. However, the approach adapted in this study is not physically practical as die bottom surface is also where heat is applied, making temperature measurements no possible there using IR thermometry.

Beside deterministic methods, statistical frameworks for the solution of inverse heat conduction problems are also available in the literature. Bayesian framework stands out in the literature as a statistical approach for the solution of inverse heat transfer problems. A statistical approach is preferred rather than deterministic solution in [43], where a Bayesian framework is used to estimate spatially distributed thermal properties and heat transfer coefficient simultaneously using thermal tomography. The feasibility of the model developed is tested experimentally for a cylindrical prototype including a through hole, where temperature sensors are placed at the side area of the cylinder [44]. Results show that estimations demonstrate cavity location. While numerical case study results in more accurate estimations compared to experimental data, the study shows the feasibility of the method proposed in [43]. Wang and Zabaras [45] use Bayesian approach for inverse heat conduction problem in order to estimate boundary heat flux and measurement noise, considering a 1-D and a 2-D case. They show that Bayesian approach is satisfactory even when measurement data is small. Gnanasekeran and Balaji [46] estimated average surface heat transfer coefficient and thermal conductivity of a vertical flat fin using thermocouple readings in a steady state natural convection experiment. The problem is formulated as 1-D and thermal quantities to be estimated are assumed to be constant. Experimental data is used for the inverse problem solution. Optimum number of measurements for a desirable accuracy is also studied in [46]. Results show that even nine thermocouples can provide estimations with high accuracy. Yet, when the number of measurements is less than nine, standard deviation of estimations increases non-linearly. Kaipo and Fox [47] provide a review of applications of Bayesian approach for inverse heat transfer problems. As Kaipo and Fox [47] state, Bayesian framework aims at characterizing

uncertainties in estimations, which differentiates it from deterministic methods, meaning that Bayesian approach provides point estimates with reliability assessment and posterior uncertainty. Rather than adapting a Gaussian noise model as generally practiced in deterministic methods, Bayesian models measurement uncertainties considering system specific probability of the event as explained in detail in [47]. Literature review indicates that Bayesian provides probabilistic answers with higher accuracy compared to deterministic methods [44-48]. However, implementation of Bayesian framework is a tedious task. It is very computationally extensive, especially for multi-dimensional problems. Therefore, one needs to consider the level of accuracy needed when making a decision between deterministic and statistical approach. It can be inferred from the literature review that deterministic methods are more suitable when extremely fine visual image is not required.

In this study, thermal tomography is applied to a high density interconnect flip chip package, where spreading is effective due to different sized IHS and die. The input signal is provided by the die and IR camera readings of temporal temperature distribution at the top surface of his is used as measured response. The objective is to characterize defects on thermal interface material quantitatively to detect defect location and size. Levenberg-Marquardt algorithm is used as an image reconstruction technique to solve the resulting inverse problem, considering its simplicity and efficiency in terms of computational time.

2. PROBLEM STATEMENT AND FORMULATION

2.1. Problem Statement

Microelectronic package with its standard cooling solution, an air cooled heat sink, is illustrated in Figure 2.1. During the assembly process development, many prototype packages are produced to understand the adequacy of different assembly process recipes. These packages are tested by following a standard test procedure using the system shown in Figure 2.1. If the measured junction to air thermal resistance in the standard thermal test (Test-1) exceeds the specified value, it means that the package thermal resistance is above the desired value due to existing defects within the package. In regular development procedure, the defect in the package is identified by the qualitative approaches mentioned earlier (CSAM or X-ray). As it is proposed to identify the defect via thermal tomography in this study, a second thermal test (Test-2) is performed on the package as shown in Figure 2.2.

Test-2 is comprised of heating the package using a short pulse and capturing the transient thermal image over the IHS (Figure 2. 2) using an IR camera. In order to obtain IR images, heat sink used in the standard thermal test shown in Figure 2.1 is removed and constant, uniform die power of 120 W is applied for the duration of 100 ms following a 0.5 ms long ramp-up period. The captured thermal images of IHS top surface are then used to reproduce the image of the TIM1 layer through image reconstruction algorithms. The testing system consists of a heating source, IR camera, data acquisition and image processing system [26].

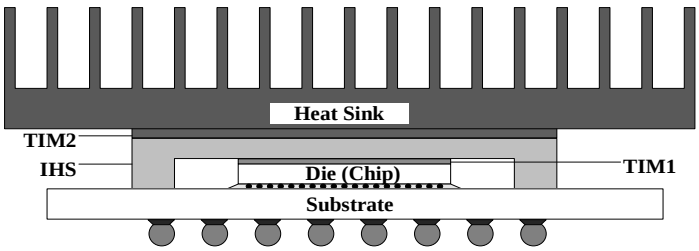

Figure 2.1. Electronic package used in thermal performance test (Test-1)

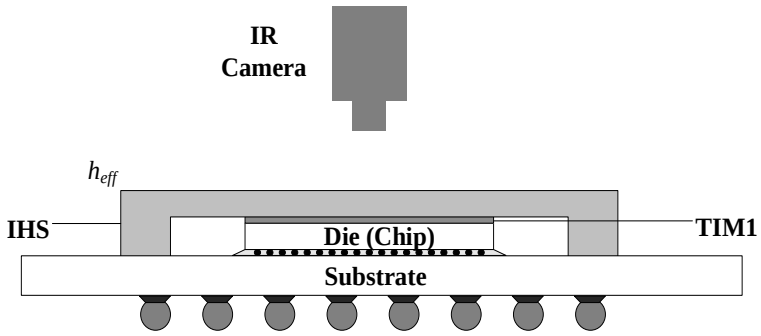

Figure 2.2. Electronic package used in thermal tomography (Test-2)

The objective of the current study is to demonstrate the concept theoretically. Therefore, the study is carried out via numerical simulations. Hence, the geometries of both tests are simplified for thermal simulations as shown in Figure 2.3 and Figure 2.4. For the standard thermal test (Test-1), only the heat sink base is considered as shown in Figure 2.3, and an effective heat transfer coefficient (h_{eff}) of 1460 W/m^2-K is used to represent a typical reference heat sink performance. Similar simplification is adapted for IHS for both tests. It is assumed that the heat transfer coefficient due to forced convection over exposed IHS is 200 W/m^2-K. Uniform die power of q''=120 W with 0.5 ms ramp-up time is applied until the system reaches steady state for Test-1, whereas same power is applied for 100 ms for Test-2. For both tests, the ambient is assumed to be 25°C. The heat transfer through the rest of the system is assumed to be negligible. The geometry and the material properties of the components of the package are presented in Table 2.1. The presented values are in agreement with the values proposed in [2, 48]. Heat sink and IHS are made of copper. TIM1 and TIM2 materials are considered as G1 and G9 as suggested in [48], respectively and die material is silicon.

Test-2 is conducted by capturing thermal images of top surface of IHS with 10ms intervals during 100 ms of heating in order to detect defects both qualitatively and quantitatively. It was observed that for the package considered in this study, the signal smears after approximately 100 ms due to spreading effect. It was also observed that shorter experiment duration results in poorer estimations as insufficient measurement data does not fully reflect system response. Discrete temperature data obtained from the captured thermal images for 225 points across the IHS top surface is then used as measurement data. Described

measurement can be performed by a thermal camera with 320x256 pixel resolution and 240 Hz frequency.

As the objective of the study is to identify the feasibility of the method for package fault detection, the study is carried out numerically replacing experimental data with numerical experiments. Experimental data is subject to some error due to measurement uncertainties. As tomography problems are ill-posed, any small perturbation in the input data may cause significant changes in the solution. In order to simulate experimental data, random measurement error is introduced to thermal simulations as suggested by [34]. The random error is introduced using pseudo-random numbers based on Gaussian distribution considering the standard deviation of the IR camera used. The measurement uncertainty limit for IR cameras is available in the literature such as [49]. In addition to measurement noise, other uncertainties such as uncertainty in the thermal properties of the materials, power applied and convective heat transfer coefficient are taken into account in the simulations. For the simulated problem, the uncertainties in the thermal properties of die, TIM, IHS as well as uncertainty in power applied and convective heat transfer are considered as 2%, 0.35%,3%,0.2% and 10%, respectively as suggested in [50, 48, 51-53], respectively.

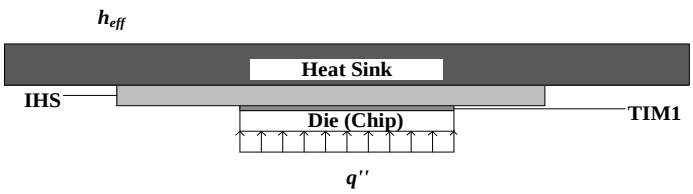

Figure 2.3. Simplified version of electronic package model used in thermal performance test simulations

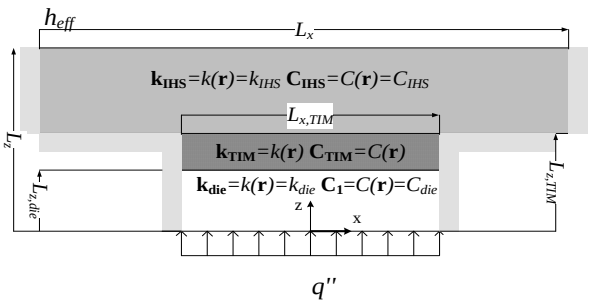

Figure 2.4. Simplified version of electronic package model used in thermal tomography simulation (dimensions not to scale)

Table 2.1. Component material properties

Component	Size [mm^3]	k [W/m-K]	c_p [J/kg-K]	ρ [kg/m^3]
Heat Sink	80x80x7.5	400	390	8960
TIM2	30x30x1.5	2.87	767	2500
IHS	30x30x1.5	400	390	8960
TIM1	10x10x0.09	5	876	2500
Die	10x10x0.75	141.2	700	2330

2.2. Direct Problem Formulation

Direct problem is solved in order to simulate temperature measurement data obtained from thermal tomography. Direct problem can be formulated by the heat conduction equation and for the system presented in Figure 2.4, it is given as:

$$\nabla.\left[k(\mathbf{r})\nabla T(\mathbf{r},\mathbf{t})\right] = C(\boldsymbol{r})\frac{\partial T(\mathbf{r},\mathbf{t})}{\partial t} \tag{2.1}$$

where $\mathbf{r}$= [x y z].

Initial condition is defined as:

$$T(\mathbf{r},0) = T_{\infty} \tag{2.2}$$

Boundary conditions are as follows:

$$-k(\mathbf{r})\left(\frac{\partial T}{\partial z}\right)_{\mathbf{z}=0} = q'',\ |x| \le L_{x,die}/2,\ |y| \le L_{y,die}/2 \tag{2.3}$$

$$\left(\frac{\partial T}{\partial z}\right)_{z\ =\ L_{z,TIM}} = 0,\ |x| > L_{x,die}/2, |y| > L_{y,die}/2 \tag{2.4}$$

$$\left(\frac{\partial T}{\partial x}\right)_{x=\pm L_{x,die}/2} = 0,\ 0 \le z \le L_{z,TIM},\ |y| \le L_{y,die}/2 \tag{2.5}$$

$$\left(\frac{\partial T}{\partial x}\right)_{x=\pm L_{x}/2} = 0,\ L_{z,TIM} \le z \le L_{z},\ |y| \le L_{y}/2 \tag{2.6}$$

$$\left(\frac{\partial T}{\partial y}\right)_{y=\pm L_{y,die}/2} = 0,\ 0 \le z \le L_{z,TIM},\ |x| \le L_{x,die}/2 \tag{2.7}$$

$$\left(\frac{\partial T}{\partial y}\right)_{y=\pm L_{y}/2} = 0,\ L_{z,TIM} \le z \le L_{z},\ |x| \le L_{x}/2 \tag{2.8}$$

$$-k(\mathbf{r})\left(\frac{\partial T}{\partial z}\right)_{z=L_z} = h_{eff}\left[T(\mathbf{r},\mathbf{t}) - T_{\infty}\right],\ |x| \le L_x/2, |y| \le L_y/2 \tag{2.9}$$

Interface boundary conditions are defined as:

$$-k_i(\mathbf{r})\left(\frac{\partial T}{\partial z}\right)_{z=L_{z,i}^-} = -k_j(\mathbf{r})\left(\frac{\partial T}{\partial z}\right)_{z=L_{z,i}^+} \tag{2.10}$$

$$T\left(x,y,L_{z,i}^-,t\right) = T\left(x,y,L_{z,i}^+,t\right) \tag{2.11}$$

where (i, j) pair is either (die, TIM) or (TIM, IHS). Equations 2.10 and 2.11 are defined in the range: $|x| \le L_{x,die}/2$, $|y| \le L_{y,die}/2$. $L_{z,i}^-$, $L_{z,i}^+$ represents values obtained approaching $L_{z,i}$ from $+z$ and $-z$ directions, respectively.

All the properties are known in the system for the direct problem. For a given power map and convection boundary condition, temperature distribution in the system is obtained from the solution of direct problem. Various numerical solution methods can be used to solve the direct problem [54]. A commercial finite element software (COMSOL Multiphysics) is used as a solver in this study.

Defects due to contaminations are not considered in this study; therefore, void properties are considered to be identical to air properties. Considering this assumption, void fraction is defined in order to save computational time and estimate k_{TIM} and C_{TIM} simultaneously. The void fraction in a control volume is defined as:

$$\varphi = \frac{V_v}{V} \tag{2.12}$$

where V_v is the volume of the void out of total volume V in a control volume, and void fraction is defined in [0,1] range. The length of void fraction vector, $\boldsymbol{\varphi}$, is equal to number of unknown parameters to be estimated, Nu=121. The effective heat capacity for a voided volume of TIM material can be defined as:

$$C_{TIM} = C_v\varphi + (1-\varphi)C_{TIM,ideal} \tag{2.13}$$

and similarly, effective thermal conductivity for a voided volume of TIM is defined by weighted arithmetic mean of conductivities as Sweat [55] proposes:

$$k_{TIM} = k_v\varphi + (1-\varphi)k_{TIM,ideal} \tag{2.14}$$

Thermal conductivity model proposed by Sweat [55] is validated in [56] where a 3-D numerical model created using actual voids predicts similar results as the 3-D model using a volume-average- effective thermal conductivities of TIM.

For given void fraction distribution, $\boldsymbol{\varphi}_\mathbf{n}=[\varphi_1, \varphi_2,\ldots, \varphi_{Nu}]^T$, where n=[1,2,…, Nu], unknown property distributions, k_{TIM} and C_{TIM} can be defined from Equations 2.13 and 2.14. Measurement operator which represents temperature data obtained from IR camera can be defined as:

$$\mathbf{T_m}(\boldsymbol{\varphi}) = T(\mathbf{r_s}, \mathbf{t_m}) \tag{2.15}$$

Equation 2.15 represents temperature estimated by the solution of the direct problem at the sensor locations and at selected measurement times. Corresponding vectors $\mathbf{r_s}$, measurement location vector, and $\mathbf{t_m}$, measurement time vector, are defined as in Equation 2.16 and Equation 2.17, respectively.

$$\mathbf{r}_s = \begin{bmatrix} r_{s,1} \\ r_{s,2} \\ \vdots \\ r_{s,N_S} \end{bmatrix} \tag{2.16}$$

$$\mathbf{t_m} = \begin{bmatrix} t_{m,1} \\ t_{m,2} \\ \vdots \\ t_{m,N_t} \end{bmatrix} \tag{2.17}$$

2.3. Inverse Problem Formulation

Despite their conceptual differences, inverse and optimization problems have a lot in common. Therefore, inverse problems can be regarded as optimization problems. Unknown void fraction distribution in the TIM, $\boldsymbol{\varphi}$, can be estimated by minimizing the objective function, which is the least squares norm of the difference between measured temperatures obtained from IR camera sensors, $\mathbf{Y}=Y(\mathbf{r_s},\mathbf{t_m})$ measured at location $\mathbf{r}_{s.i}$ at time $\mathbf{t}_{m,j}$, where $\mathbf{i}=[1,2,.., N_s]$ and $\mathbf{j}=[1,2,\ldots,N_t]$, and estimated temperatures, $\mathbf{T_m}(\boldsymbol{\varphi})=T\ (\mathbf{r_s},\mathbf{t_m})$. Objective function is defined as least squares norm of the difference between measured and estimated temperatures:

$$F(\boldsymbol{\varphi}) = \frac{1}{2}[\mathbf{Y} - \mathbf{T_m}]^{\mathrm{T}}[\mathbf{Y} - \mathbf{T_m}] \tag{2.18}$$

The minimum of the objective function is where the gradient with respect to unknown void fraction vector,φ, is equal to zero, which is represented in Equation 2.19:

$$\nabla F(\boldsymbol{\varphi}) = \left[-\frac{\partial \mathbf{T_m}}{\partial \boldsymbol{\varphi}} \right]^{\mathrm{T}} [\mathbf{Y} - \mathbf{T_m}] = 0 \tag{2.19}$$

Jacobian matrix indicates the effect of change in void fraction on temperature distribution of the system. In the Jacobian calculation, the effect of void fraction change for *Nu* unknown void fraction values on $N_s N_t$ temperature measurements is considered. Jacobian matrix that contains sensitivity coefficients of the system can be defined as:

$$\mathbf{J}(\boldsymbol{\varphi}) = \left[\frac{\partial \mathbf{T_m}^{\mathrm{T}}}{\partial \boldsymbol{\varphi}} \right]^{\mathrm{T}} = \begin{bmatrix} \frac{\partial T_{m,1}}{\partial \varphi_1} & \cdots & \frac{\partial T_{m,1}}{\partial \varphi_{Nu}} \\ \vdots & \frac{\partial T_{m,l}}{\partial \varphi_k} & \vdots \\ \frac{\partial T_{m,NsNt}}{\partial \varphi_1} & \cdots & \frac{\partial T_{m,NsNt}}{\partial \varphi_{Nu}} \end{bmatrix} \tag{2.20}$$

Jacobian calculation is performed using forward finite difference approximation as suggested in [34]:

$$J_{mn} \cong \frac{T_m(\varphi_1, \varphi_2, ..., \varphi_n + \Delta\varphi_n, ..., \varphi_{Nu}) - T_m(\varphi_1, \varphi_2, ..., \varphi_n, ..., \varphi_{Nu})}{\Delta\varphi_n} \tag{2.21}$$

Equation 2.19 can be re-written using the Jacobian matrix as:

$$-\mathbf{J}(\boldsymbol{\varphi})^{\mathrm{T}} [\mathbf{Y} - \mathbf{T_m}(\boldsymbol{\varphi})] = 0 \tag{2.22}$$

2.4. Levenberg-Marquardt Algorithm (LMA)

Different solution techniques for the solution of non-linear inverse problem defined in Equation 2.22 are summarized in Section 1.2 and explained in detail in [35, 58]. In this study Levenberg-Marquardt method is used due to its efficiency in terms of computation time and accuracy [4].

The Taylor series expansion of $\mathbf{T_m}(\boldsymbol{\varphi}')$ if $\boldsymbol{\varphi}$ is in the neighborhood of $\boldsymbol{\varphi}'$, the exact solution of Equation 2.22, can be written as [4]:

$$\mathbf{T_m}(\boldsymbol{\varphi}') = \mathbf{T_m}(\boldsymbol{\varphi}) + (\boldsymbol{\varphi}' - \boldsymbol{\varphi})\frac{\partial \mathbf{T_m}(\boldsymbol{\varphi})}{\partial \boldsymbol{\varphi}} + \cdots \tag{2.23}$$

In order to calculate $\boldsymbol{\phi}'$, Equation 2.23 can be rewritten by neglecting higher order terms, and representing the gradient term using the Jacobian:

$$\mathbf{J}(\boldsymbol{\varphi})(\boldsymbol{\varphi}' - \boldsymbol{\varphi}) = [\mathbf{Y} - \mathbf{T_m}(\boldsymbol{\varphi})] \tag{2.24}$$

considering $\mathbf{Y}=\mathbf{T_m}(\boldsymbol{\varphi}')$.

Multiplying both sides of Equation 2.24 with $\mathbf{J}(\boldsymbol{\varphi})^{\mathrm{T}}$ results in:

$$\mathbf{J}(\boldsymbol{\varphi})^{\mathrm{T}}\mathbf{J}(\boldsymbol{\varphi})(\boldsymbol{\varphi}' - \boldsymbol{\varphi}) = \mathbf{J}(\boldsymbol{\varphi})^{\mathrm{T}}[\mathbf{Y} - \mathbf{T_m}(\boldsymbol{\varphi})] \tag{2.25}$$

Iterative solution of Equation 2.25 is known as Newton-Gauss method. If the problem is well-posed and the matrix $\mathbf{J}(\boldsymbol{\varphi})^{\mathrm{T}}\mathbf{J}(\boldsymbol{\varphi})$ is non-singular, Newton-Gauss method converges. However, inverse problems are usually ill-posed, and $\mathbf{J}(\boldsymbol{\varphi})^{\mathrm{T}}\mathbf{J}(\boldsymbol{\varphi})$ is singular and regularization of the system is required. Levenberg-Marquardt algorithm regularizes the system by modifying the singular matrix $\mathbf{J}(\boldsymbol{\varphi})^{\mathrm{T}}\mathbf{J}(\boldsymbol{\varphi})$ by $\mathbf{J}(\boldsymbol{\varphi})^{\mathrm{T}}\mathbf{J}(\boldsymbol{\varphi})+\lambda\boldsymbol{\Omega}$, which results in:

$$[\mathbf{J}(\varphi)^T \mathbf{J}(\varphi) + \lambda\mathbf{\Omega}](\varphi' - \varphi) = \mathbf{J}(\varphi)^T[\mathbf{Y} - \mathbf{T_m}(\varphi)] \tag{2.26}$$

The conditioning matrix is chosen as $\mathbf{\Omega}$=diag[$\mathbf{J}(\varphi)^T\mathbf{J}(\varphi)$], a diagonal matrix with diagonal elements of $\mathbf{J}(\varphi)^T\mathbf{J}(\varphi)$. For large damping parameters, λ, Levenberg-Marquardt algorithm converges according to gradient decent method while it approaches to Newton-Gauss method when damping parameter small. Levenberg-Marquardt algorithm used in this study is presented in Figure 2.5.

i) Choose an initial guess φ^0 for the solution of φ, set k=0.

ii) Solve direct problem for $\mathbf{T_m}(\varphi^k)$ in COMSOL (Equation 2.1-2.15).

iii) Calculate $F(\varphi^k)$ (Equation 2.18).

iv) While $F(\varphi^k) > \varepsilon_1$,compute $\mathbf{J}(\varphi^k)$ (Equation 2.20-2.21) and

$\mathbf{\Omega}(\varphi^k)$=diag $(\mathbf{J}(\varphi^k)^T\mathbf{J}(\varphi^k))$.

v) Estimate φ^{k+1} solving:

$$\varphi^{k+1} = \varphi^k + [\mathbf{J}(\varphi^k)^T\mathbf{J}(\varphi^k) + \lambda^k \mathbf{\Omega}(\varphi^k)]^{-1}\mathbf{J}(\varphi^k)^T[\mathbf{Y} - \mathbf{T_m}(\varphi^k)] .$$

vi) Calculate $\mathbf{T_m}(\varphi^{k+1})$ and $F(\varphi^{k+1})$ using new estimate.

vii) If $F(\varphi^{k+1}) - F(\varphi^k) > \varepsilon_2$, replace λ^k by $10\lambda^k$ and return to step (iii).

Else, accept the new estimate. Replace λ^k by $0.1\lambda^k$ and k by k+1 and return to step (iv).

Figure 2.5. Levenberg-Marquardt algorithm (Adapted from [34])

As explained in Section 2.1, effect of other uncertainties such as uncertainty in thermal properties of die, thermal interface material, integrated heat spreader as well as power applied and convective heat transfer coefficient is considered when random measurement error based on Gaussian distribution is added to temperature measurements. These uncertainties are taken into account as follows [58]:

$$\sigma_s(\mathbf{r_s},\mathbf{t_m})^2 = \sum_{\mathbf{i}} \left[\frac{\partial T(\mathbf{r_s},\mathbf{t_m})}{\partial p_i} \sigma_{pi} \right]^2 \tag{2.27}$$

where p and σ_p are the properties and boundary conditions mentioned above and related uncertainties, respectively. σ_s represents the uncertainty due to properties and boundary conditions.

In order to understand ill-posed nature of the problem singular value decomposition (SVD) is performed as suggested in [59]. SVD of a matrix **A** is defined as:

$$\mathbf{A} = \mathbf{USV}^{\mathrm{T}} \tag{2.28}$$

where **A** is an **M**×**N** matrix, **U** and **V** are M×M and N×N orthogonal matrices and **S** is the diagonal matrix containing singular values of the matrix **A**. Condition number (C_N) of **A** is defined as the ratio of its largest singular value to its smallest singular value, as in Equation 2.26.

$$C_N = \frac{\max(\mathbf{S})}{\min(\mathbf{S})} \tag{2.29}$$

The larger the condition number, the more ill-posed the system [60]. In order to understand regularization effect on the system, condition numbers for the matrices $\mathbf{J}(\varphi)^{\mathrm{T}}\mathbf{J}(\varphi)$ and $[\mathbf{J}(\varphi)^{\mathrm{T}}\mathbf{J}(\varphi)+\lambda\mathbf{\Omega}]$ are computed and compared.

After identifying ill-posed nature of the system, a regularization parameter λ must be selected in order to regularize the system while maintaining physics of the problem. Hansen [59] proposes the so-called “L-curve” as a useful graphical tool in order to decide on regularization parameter. L-curve illustrates the trade-off between the norm of the regularized solution and the norm of the residual, represented in Equation 2.30 and Equation 2.31, respectively.

In order to choose the optimum regularization parameter, L-curve is plotted for a range of regularization parameters. When plotted in log-log scale for discrete ill-posed problems, L-curve has a distinct corner, which separates vertical and horizontal axes as shown in Figure 2.6. Increasing regularization parameter filters more singular values in the system, which in turn increases residual error while solution norm decreases. Hansen [60] proposes that optimum regularization parameter, which balances both solution and residual norm, corresponds to the corner of the L-curve. In practical cases where we do not observe a distinct corner, the damping coefficient, which keeps both solution and residual norm close to the corner, can be chosen as the optimal one.

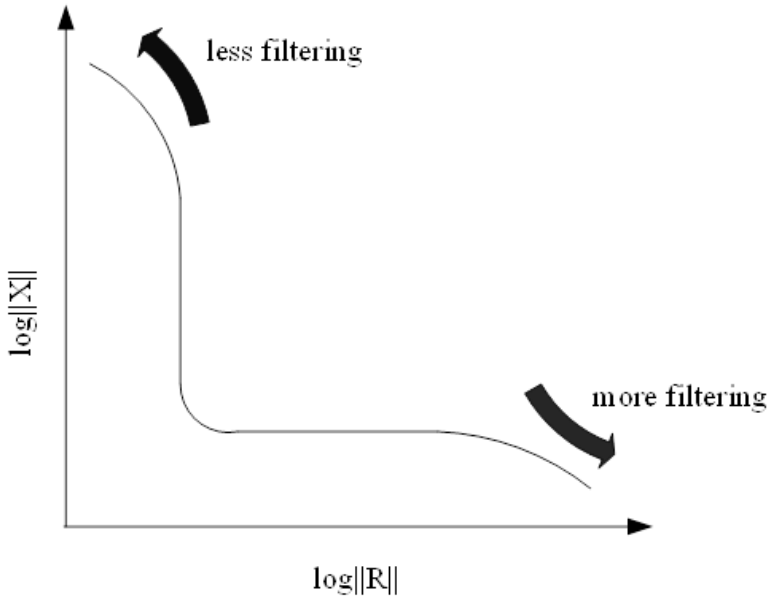

Figure 2.6. L-curve form for discrete inverse problems (Adapted from [59])

$$\mathbf{X} = (\boldsymbol{\varphi}' - \boldsymbol{\varphi}) = [\mathbf{J}(\boldsymbol{\varphi})^{\mathrm{T}}\,\mathbf{J}(\boldsymbol{\varphi}) + \lambda\boldsymbol{\Omega}]^{-1}\{\mathbf{J}(\boldsymbol{\varphi})^{\mathrm{T}}[\mathbf{Y} - \mathbf{T_m}(\boldsymbol{\varphi})]\} \tag{2.30}$$

$$\mathbf{R} = [\mathbf{J}(\boldsymbol{\varphi})^{\mathrm{T}}\,\mathbf{J}(\boldsymbol{\varphi})](\boldsymbol{\varphi}' - \boldsymbol{\varphi}) - \{\mathbf{J}(\boldsymbol{\varphi})^{\mathrm{T}}[\mathbf{Y} - \mathbf{T_m}(\boldsymbol{\varphi})]\} \tag{2.31}$$

2.5. Stopping Criteria

If the measurement errors and other uncertainties are not introduced to simulated data, then the resulting solution is referred as so-called “inverse crime”. Stopping criteria for the solution of inverse crime case using Levenberg-Marquardt algorithm is defined as:

i) $F(\varphi^k) \leq \varepsilon_1$ (2.32)

ii) $F(\varphi^{k+1}) - F(\varphi^k) \leq \varepsilon_2$ (2.33)

where $\varepsilon_1 = \varepsilon_2 = 10^{-5}$ in the algorithm implemented. The algorithm continues iterations until both Equation 2.32 and Equation 2.33 are satisfied. The criterion in Equation 2.32 is to check whether the least squares norm of the measured and calculated temperature is small enough, whereas Equation 2.33 checks the convergence of the algorithm. If Equation 2.33 is not satisfied, damping coefficient is modified and the algorithm continues.

In reality, all measurements are subjected to measurement error. In this study, random measurement error based on Gaussian (normal) distribution is introduced. Figure 2.7 represents probability density function of the normal distribution, where *f(x)* represents frequency of occurring of the corresponding event *x*.

The probability density function, $f(x)$ is defined as:

$$f(x) = \frac{1}{\sqrt{2\pi}} e^{-(x-\mu)^2/2\sigma^2} \tag{2.34}$$

where x is defined in the interval $[-\infty\ \infty]$ and, μ and σ represents the mean and standard deviation, respectively [60]. Figure 2.7 is a normalized curve of Gaussian distribution with zero mean. Sum of squares of errors (SSE) of temperature measurements for our problem with zero mean (μ=0) is calculated as:

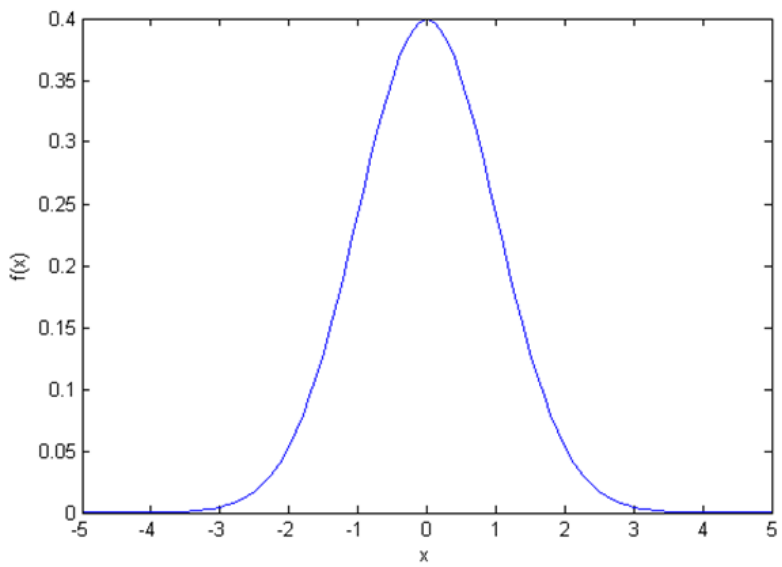

Figure 2.7. Probability density function of the normal distribution

$$SSE = \sum_{i}^{N_s N_t} x_i^2 \tag{2.35}$$

where $N_s N_t$ is the number of observations, i.e. number of temperature measurements in the problem presented, and x_i is the ith observation. Then, considering the frequency of occuring of the measurement, $f(x)$, and total number of measurements, stopping criteria for error introduced case can be calculated as:

$$\varepsilon = \int_{0}^{\infty} x^2 [\, f(x) N_s N_t \,] dx \tag{2.36}$$

Substitution of Equation 2.34 into Equation 2.36 and carrying out the resulting integration results in Equation 2.37:

$$\varepsilon = 0.5 N_s N_t \sigma^2 \tag{2.37}$$

where σ represents the standard deviation of the error introduced to the measurements. Stopping criteria for error introduced measurements as represented in Equation 2.37 is also consistent with the stopping criteria proposed in [4, 34, 61].

3. GRID INDEPENDENCY AND MODEL VERIFICATION

As direct problem is solved using finite element method (FEM) using commercial software COMSOL Multiphysics, grid independency of the FEM model is checked first. Then, the verification of the direct (forward) problem is performed by comparing the results of FEM model with reference solution provided by Intel Corporation using ANSYS Icepak [62]. Grid independency tests are performed for both thermal performance test (Test-1) and thermal tomography (Test-2).

3.1. Grid Independency Study

The model of the electronic package used in thermal performance test (Test-1) shown in Figure 2.3 is checked for grid independency. The study is carried out using material properties represented in Table 2.1 and boundary conditions for Test-1 as specified in Section 2.1. The solution is carried out for ideal case where TIM is defect free. The study is performed for coarse, extra fine and extremely fine swept mesh using triangular elements. Details of mesh for all three cases are presented in Table 3.1. Figure 3.1 illustrates temperature distribution along x axis at die base surface (at z=0 mm) where y= 5 mm according to the coordinate system shown in Figure 2.4, for all three types of meshing. Maximum die temperatures T_j, referred as junction temperatures, for all cases are represented in Table 3.1.

Table 3.1. Mesh details of COMSOL model created for thermal performance test

Mesh Type	**Maximum Element Size [mm]**	**Minimum Element Size [mm]**	**Total Number of Nodes**	**T_j [^{o}C]**
Coarse	8	2.24	1280	82.05
Extra Fine	2.8	0.12	6845	82.05
Extremely Fine	1.6	0.016	19580	82.06

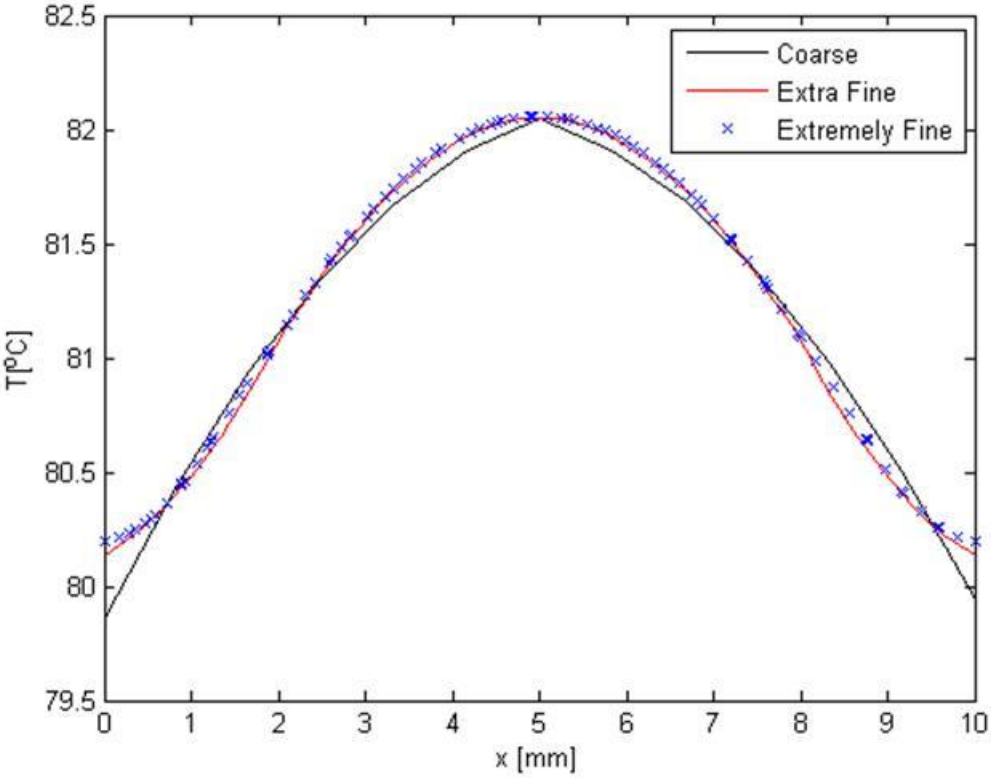

Figure 3.1. Temperature variation at die base surface (*z*=0 mm) along x axis, *y*=5 mm for thermal performance test (Test-1)

Figure 3.1 illustrates that all three types of mesh distribution shows the same trend for temperature distribution in thermal performance test (Test-1). Junction temperatures for all three cases presented in Table 3.1 do not show a remarkable difference in regards to measurement accuracy. Therefore, the numerical model created for thermal performance test (Test-1) is grid independent. The numerical model for thermal tomography (Test-2) as shown in Figure 2.4 is also tested for grid independency with meshes presented in Table 3.2. The solution is performed following the test procedure explained in Section 2.1 and TIM is considered as ideal. This study is performed for coarse, fine and extra fine swept mesh using quadrilateral elements. Die base temperature is critical to make sure that chip is not damaged during thermal tomography test,where temperature measurements are obtained from IHS top surface. Therefore, resulting temperature distributions at *t*=100 ms at the die base surface (z=0) and top surface of IHS (*z*=2.34 mm) are checked for grid independency and corresponding results are illustrated in Figure 3.2 and Figure 3.3 along x-axis where *y*=5 mm and *y*=15 mm according to the coordinate system shown in Figure 2.5, respectively.

Table 3.2. Mesh details of COMSOL model created for thermal tomography test

Mesh Type	**Maximum Element Size [mm]**	**Minimum Element Size [mm]**	**Total Number of Nodes**	**T_j [^{o}C]**
Coarse	4.5	0.84	432	61
Fine	2.4	0.3	992	60.99
Extra Fine	1.05	0.045	4892	60.99

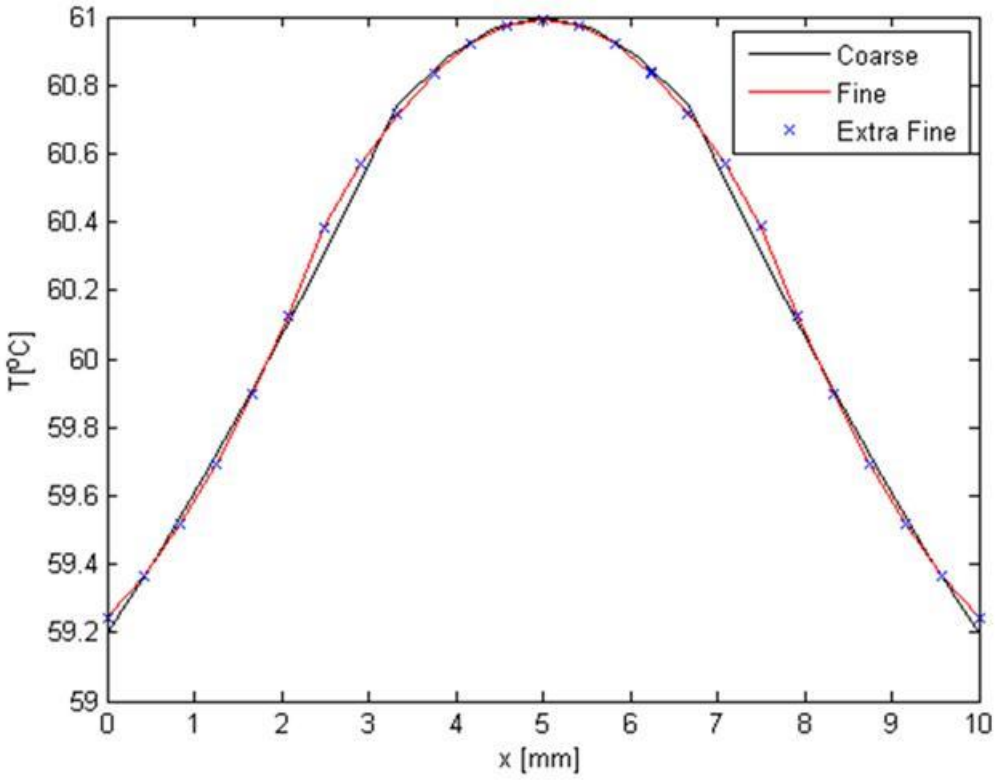

Figure 3.2. Temperature distribution at die bottom surface (z=0 mm) at t=100ms along x axis, y=5 mm for thermal tomography (Test-2)

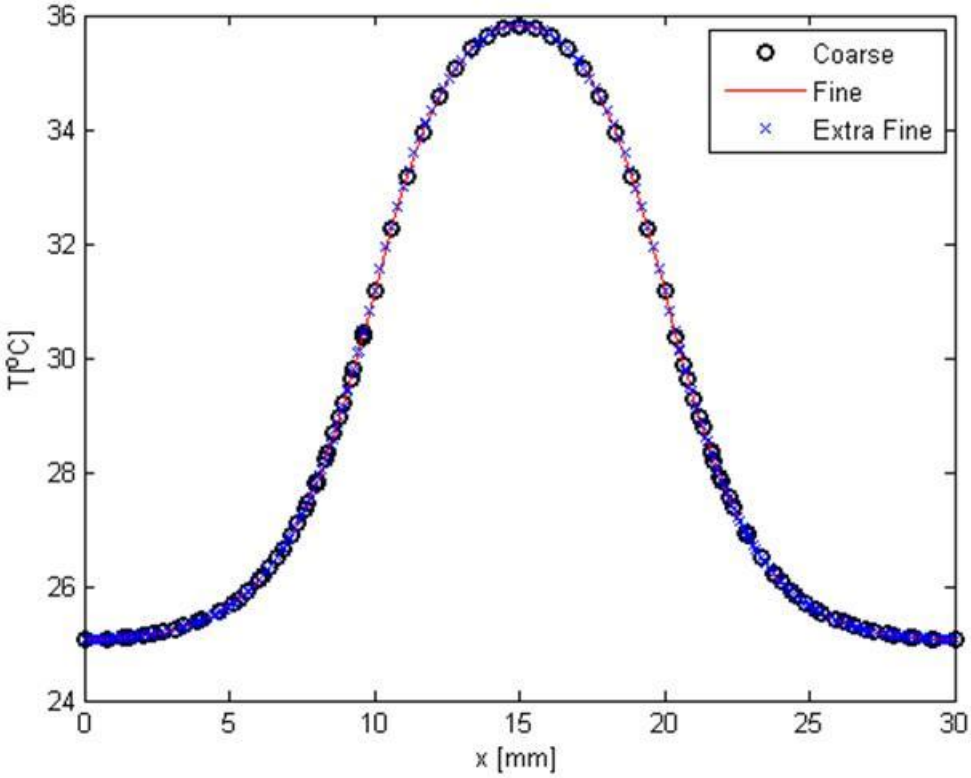

Figure 3.3. Temperature distribution at IHS top surface (*z*=2.34 mm) at *t*=100 ms along x axis, *y*=15 mm for thermal tomography (Test-2)

Figure 3.2 and Figure 3.3 illustrate that all three types of mesh distributions show the same trend for temperature distribution in thermal tomography (Test-2). As Table 3.2 shows, junction temperature differences do not constitute a significant effect for test data. Results indicate that the numerical model created for thermal tomography (Test-2) is grid independent.

In this study, extra fine mesh with triangular elements and fine mesh with quadrilateral elements are used for thermal performance test (Test-1) and thermal tomography test (Test-2), respectively.

3.2. Verification Study

The FEM model for thermal performance test with extra fine grids, details of which are presented in Table 3.1, is verified using commercial software ANSYS Icepak utilizing the validated models provided by the chip manufacturer Intel as reference solutions' model [62]. Test conditions are identical with the thermal performance test explained in Section 2.1. Junction temperatures for the FEM and the reference solution models are obtained as 82.05 ^{o}C and 81.95 ^{o}C, respectively. Temperature distribution at the bottom surface of die for both COMSOL and Icepak model is illustrated in Figure 3.4.

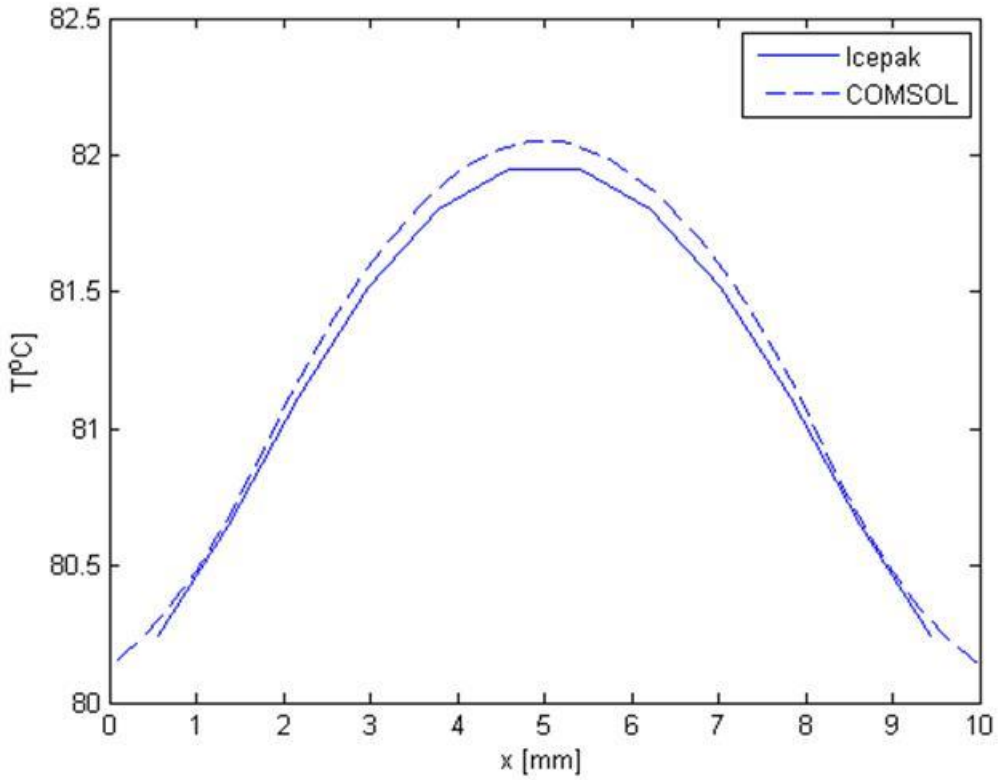

Figure 3.4. Temperature variation at die bottom surface (z=0 mm) along x axis, y=5 mm for Icepak [62] and COMSOL models for thermal performance test

4. RESULTS AND DISCUSSION

After direct solution model is verified, thermal performance test (Test-1) is applied first for several cases that differ from each other in regards to void size and location in TIM1 so that impact of void size and location on temperature rise can be investigated. Each case includes a void with a different size and at a different location in TIM1. Considering results of Test-1, a sensitivity study is created in order to relate voids size and location effect to estimation accuracy. This is followed by applying thermal tomography (Test-2) to the sensitivity study created. First, simulations are performed for the “inverse crime” case that represents the solution where no error is introduced to the simulated measurement data so that validity of the algorithm is checked. This is followed by the case where random measurement error and uncertainty is introduced to the measurement data. System ill-posedness is illustrated afterwards. Having investigated system ill-posedness, resulting void fraction estimations for the sensitivity study is presented, which is obtained utilizing Levenberg-Marquardt algorithm presented in Figure 2.5. In an effort to improve estimations, “dimensional reduction” is applied modifying the method proposed by [38]. In addition to this, LMA is modified by applying ad-hoc filtering at each iteration and reducing Jacobian size. Resulting estimations are discussed considering the effect of void size and location on estimation accuracy.

4.1. Simulated Measurements

In this study, experimental data obtained by real test equipment is simulated by solving direct heat conduction problem for the void fraction distribution created as a sensitivity study. The commercial finite element solver used in this study implements an implicit solution scheme. As a result of the grid independency study, Test-1 is performed with extra fine swept mesh with triangular elements and Test-2 is carried out with fine swept mesh with quadrilateral elements, details of which are presented in Table 3.1 and Table 3.2, respectively. Data is collected for Test-2 through transient solution for 100 ms duration with 10 ms time intervals.

Standard thermal performance test (Test-1) is simulated first to investigate whether the defect has a measureable effect on package thermal behavior. The effect of void size on

temperature rise in Test-1 is investigated one at a time, considering voids with 0.0625, 0.5 and 1 mm^2 size. In order to illustrate effect of void location on thermal performance, each void at different size is simulated at the corner, at the edge and at the center of TIM1, one at a time. Results are presented in Figure 4.1. It is observed that relatively small voids such as voids 2, 3 and 4 lead to smaller temperature rise in Test-1, indicating that their effect on thermal performance is less significant than that of voids 1 and 5. Apart from void size, void location is also an important factor affecting temperature signal in Thermal Performance Test (Test-1). For instance, void 5 at the corner causes larger temperature difference in the test compared to same sized void 1, which is located at the edge of the TIM1 surface.

Considering Test-1 results shown in Figure 4.1, a sensitivity study is constructed. A package with defected TIM1 that has a void fraction distribution shown in Figure 4.2 is considered in order to evaluate the performance of the proposed method and show void size and location effect on estimation accuracy. Center coordinates and corresponding size of the voids are presented in Table 4.1. Void fraction is equal to 0.9 at the defined coordinates.

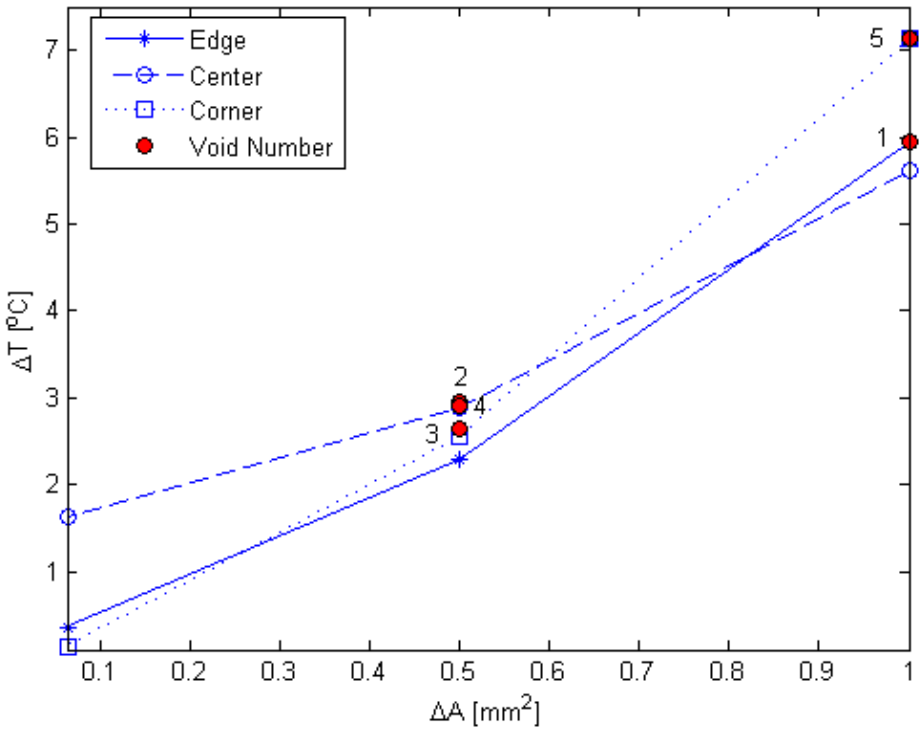

Figure 4.1. Void size and location effect on thermal performance test (Test-1)

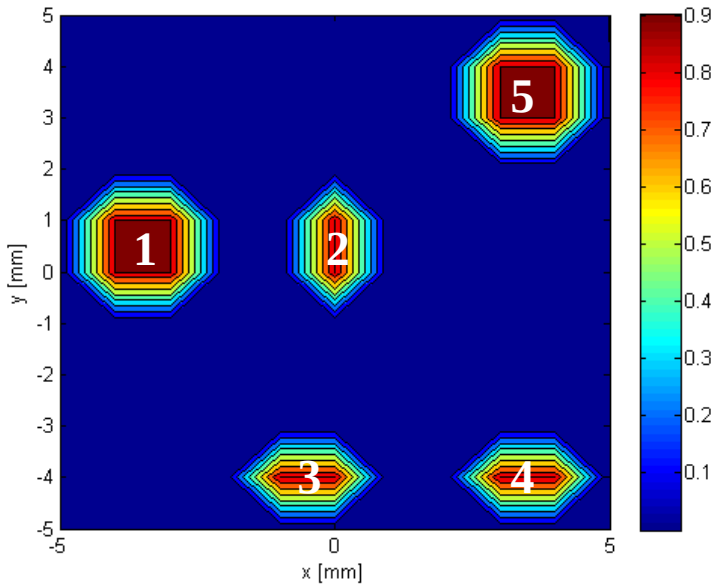

Figure 4.2. Void fraction of TIM1 used in thermal tomography test simulation

Table 4.1. Center coordinates and sizes of void fractions presented in Figure 4.2

Void Number	x [mm]	y[mm]	Area [mm^2]
1	-3.5	0.5	1
2	0	0.5	0.5
3	-0.5	-4	0.5
4	3.5	-4	0.5
5	3.5	3.5	1

Considering the measurable effect of the defect on thermal performance of the package, thermal tomography (Test-2) is performed on the electronic package. Uniform die power of 120 W is applied until the system reaches steady state at 25°C ambient temperature. Results of simulations for Test-1 for the ideal TIM1 (no defects, void fraction is 0 everywhere) and the case shown in Figure 4.2 are presented in Figure 4.3. It was observed that maximum die temperature (junction temperature) for the package with defected TIM1 layer shown in Figure 4.1 increases by 7°C with respect to that of a package with ideal TIM1 (no defects, void fraction is 0 everywhere).

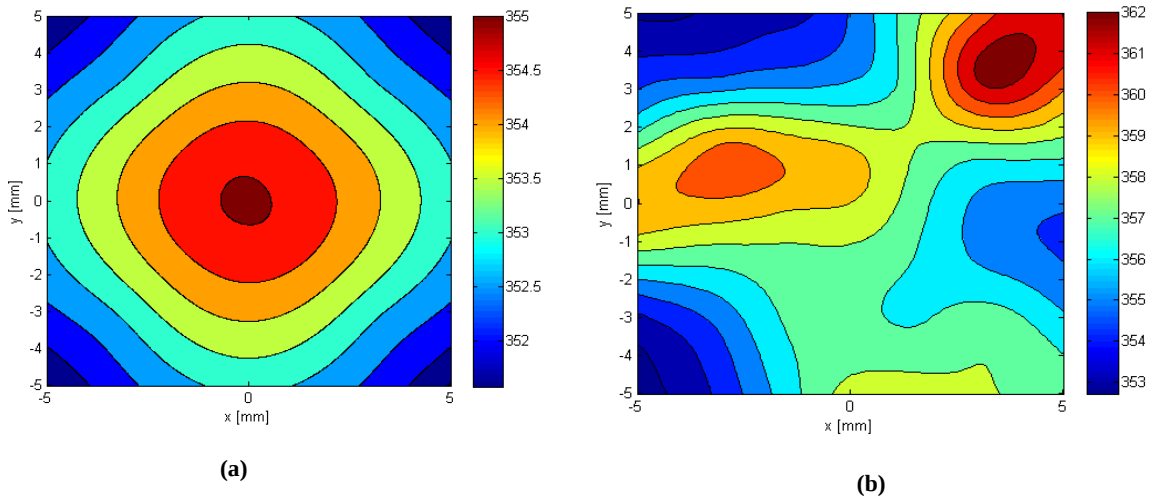

(a) **(b)**

Figure 4.3. Temperature distribution [K] at die bottom surface in thermal performance test (Test-1) for (a) ideal case, (b) case shown in Figure 4.2

Considering the measurable effect of the defect on thermal performance of the package, thermal tomography (Test-2) is performed on the electronic package. For 25°C ambient temperature, 120 W uniform die power is applied for 100 ms duration. Heat transfer coefficient over IHS is considered to be 200 W/m^2-K representing forced convection of air over top surface of IHS. Data is collected with 10 ms intervals for 100 ms duration. The estimated temperature distribution for die base and IHS is presented in Figure 4.4 and Figure 4.5, respectively. Here, Figure 4.4 represents the simulated measurement data used for thermal tomography.

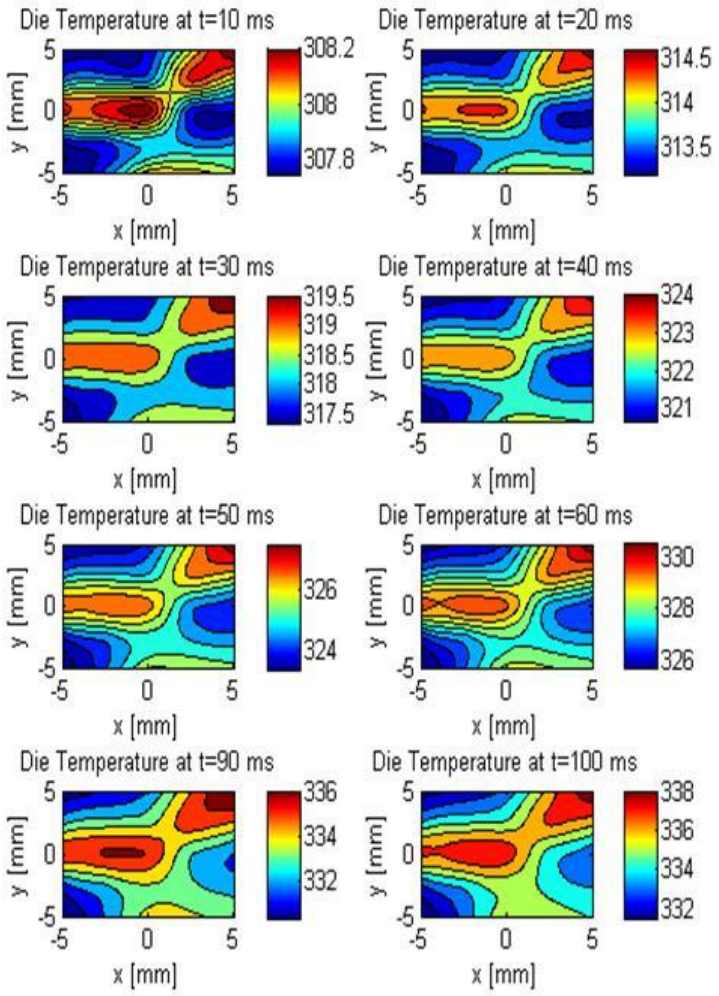

Figure 4.4. Die base temperature distribution [K] from solution of direct problem

A major characteristic of inverse problems is their unstable nature. Therefore, slight changes in input data can result in significant changes in the solution. Considering that all measurements are prone to measurement error and uncertainty, this constitutes a challenge as thermal tomography problems are inverse problems. In order to test the method synthetic measurement data that is presented in Figure 4.6 is generated by introducing random error based on measurement uncertainty to the simulated measurements presented in Figure 4.5. Here, the measurement uncertainty of 0.02^{o}C as suggested by [49] is considered. As random error is introduced with a normal distribution, 99.7% of the synthetic measurements lie within $\pm 3\sigma$ of the simulated measurements.

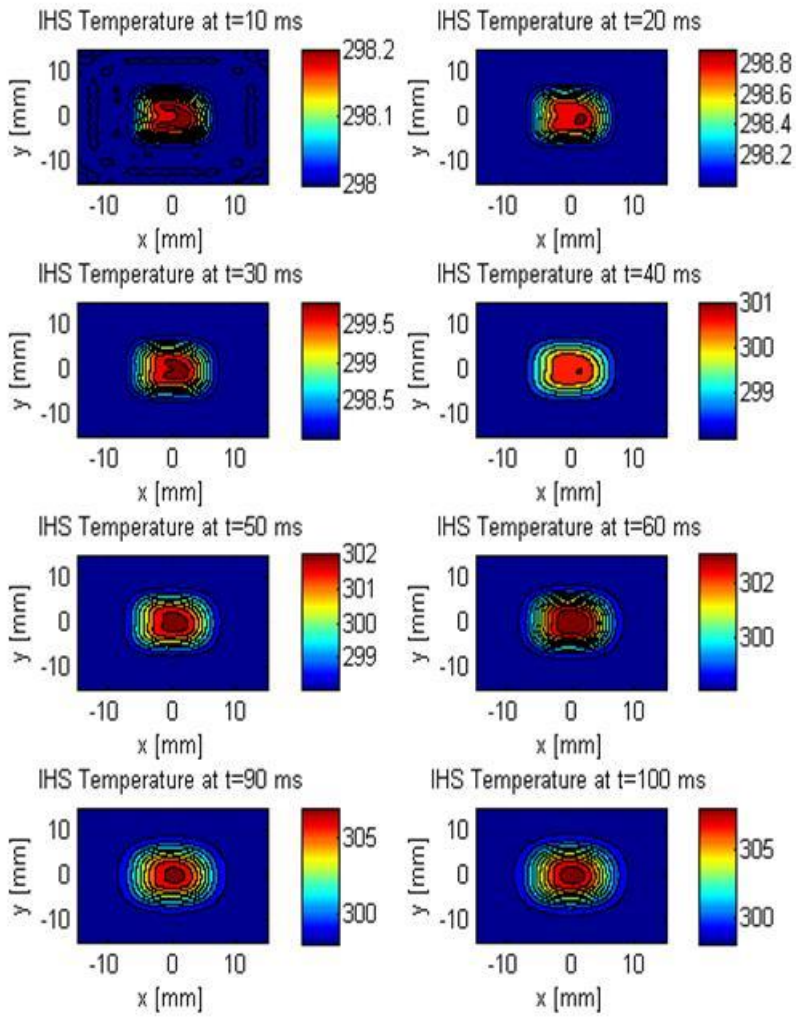

Figure 4.5. Simulated measurements, IHS temperature distribution [K] with no error estimation for the case in Figure 4.2

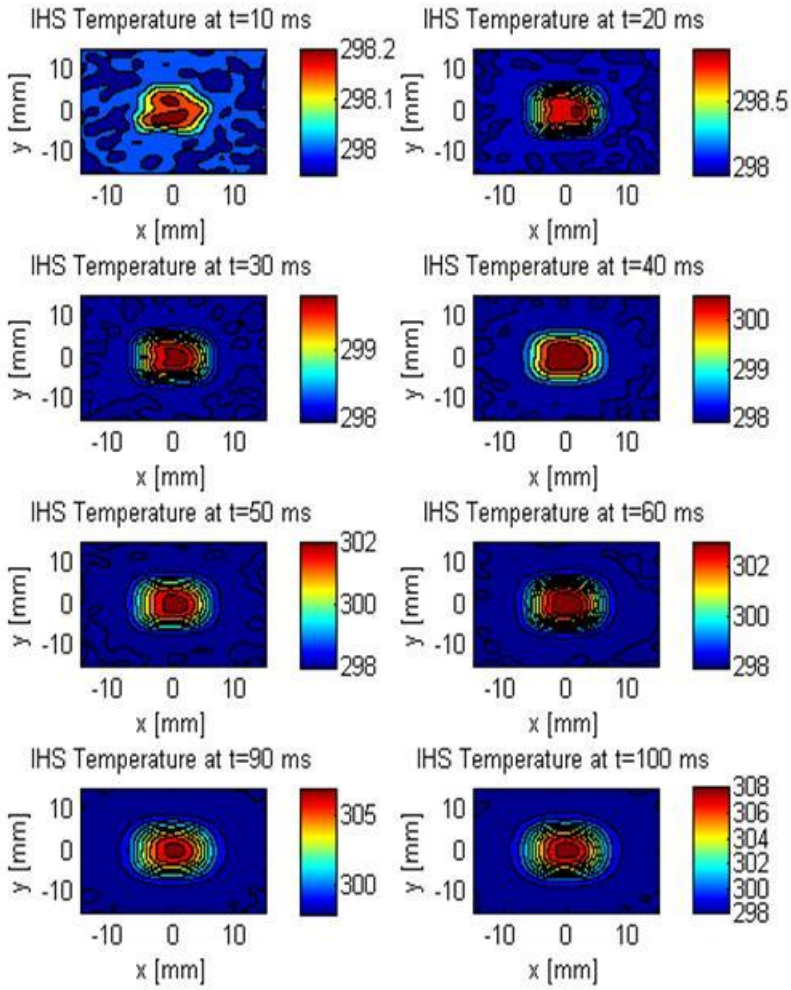

Figure 4.6. Synthetic measurement data by introducing random error and uncertainty to simulated IHS temperature distribution [K] estimation for the case in Figure 4.2

4.2. Void Fraction Estimations

Temperature data shown in Figure 4.5 and Figure 4.6 is used to quantitatively identify defects shown in Figure 4.2 by predicting the void fraction within TIM1 using Levenberg-Marquardt algorithm. The data considers test duration of 100 ms, with data collected at every 10 ms equal time steps. Total test duration is decided to reasonably represent system response by maintaining thermal signal. Defect detection using simulated measurements (Figure 4.5) is

performed that is also referred as “inverse crime” to check the validity of the algorithm before considering the more realistic or challenging case with synthetic measurement data shown in Figure 4.6.

Stopping criteria of Levenberg-Marquardt algorithm is defined as 10^{-5} for simulated measurement data (with no random measurement error introduced). Therefore, the algorithm continues iterations until both $F(\boldsymbol{\varphi})<10^{-5}$ and $F(\boldsymbol{\varphi}^{k+1})-F(\boldsymbol{\varphi}^{k})<10^{-5}$ are satisfied. For the cases using synthetic measurements, stopping criteria is defined as $0.5N_sN_t\sigma^2$ as suggested in [4, 34, 63]; σ representing the standard deviation of the measurement error introduced. Initial guess for void fraction distribution is chosen as ideal case.

Selection of the regularization parameter is critical for solution of inverse problems as higher level of regularization will introduce significant change to the original physical behavior of the system, while with smaller regularizations the system will be prone to numerical errors due to the instability that manifests itself as phantom voids in the current problem. The regularization effect of using different damping parameters can be observed by analyzing the so called “L-curve” that presents the change in norm of the solution residual with the norm of the unknown.

Ill-posedness of the system should be analyzed first in order to adjust regularization level as higher level of regularization is required to handle relatively more ill-posed systems. In order to understand nature of the problem that is represented as a linear system, singular value decomposition (SVD) can be used [59]. As explained in detail in Section 2.4, ratio of maximum to minimum singular values defines the condition number (C_N), which can be used as a metric to understand the ill-condition of the system, $C_N=\max(\mathbf{S})/\min(\mathbf{S})$. Larger C_N refers to highly ill-conditioned systems. In order to understand regularization effect on our system, the singular values for matrices $\mathbf{A}=\mathbf{J}(\boldsymbol{\varphi})^T\mathbf{J}(\boldsymbol{\varphi})$ and $\mathbf{A}_n= [\mathbf{J}(\boldsymbol{\varphi})^T\mathbf{J}(\boldsymbol{\varphi})+\lambda_n\boldsymbol{\Omega}]$, where n=1,2,3, for the case illustrated in Figure 4.2 are calculated. Resulting singular values along with corresponding condition numbers are presented in Figure 4.7. The corresponding condition numbers for $\mathbf{A}$ and $\mathbf{A}_n$, are $C_N \cong 10^{12}$, $C_{N,1} \cong 10^4$, $C_{N,2} \cong 10^3$ and $C_{N,3} \cong 30$, respectively; indicating that the system is highly ill-conditioned unless it is regularized. However, using large damping coefficient yields

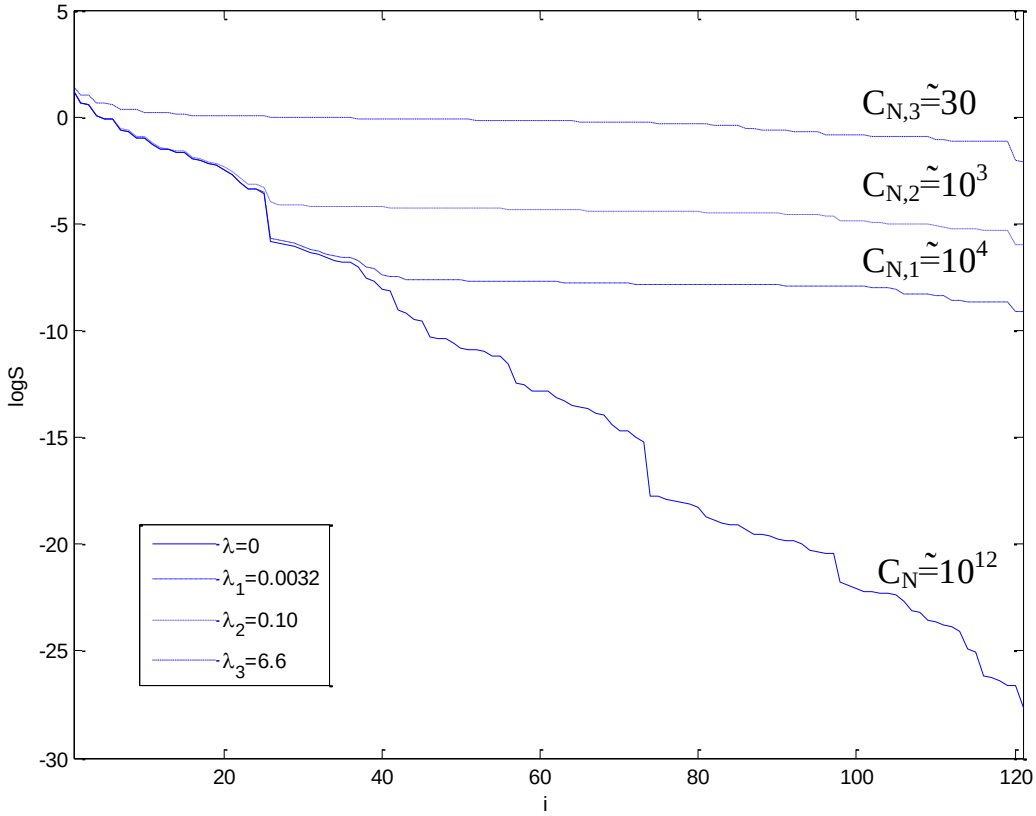

Figure 4.7. Singular value decomposition (SVD) for the case in Figure 4.2

to small condition numbers of the modified system $\mathbf{A}_n$ that would introduce a larger regularization error as system characteristics is highly altered.

Having observed the ill-posed nature of the problem, the effect of regularization on the system can be analyzed further with an L-curve. The L-curve for the first iteration is presented for $10^{-4}<\lambda<50$ range in Figure 4.8. The initial damping parameter selected is presented as λ_2=0.1 in Figure 4.11, and it keeps both solution norm and residual norm at reasonably small values [59]. In other words, the initial damping parameter chosen, λ_2=0.1, maintains a balance between the stabilizing the noise associated with random error introduced and the regularization error introduced.

The inverse problem is formulated as estimation of void fraction distribution. The most computationally expensive step of LMA is the calculation of Jacobian matrix. Jacobian matrix

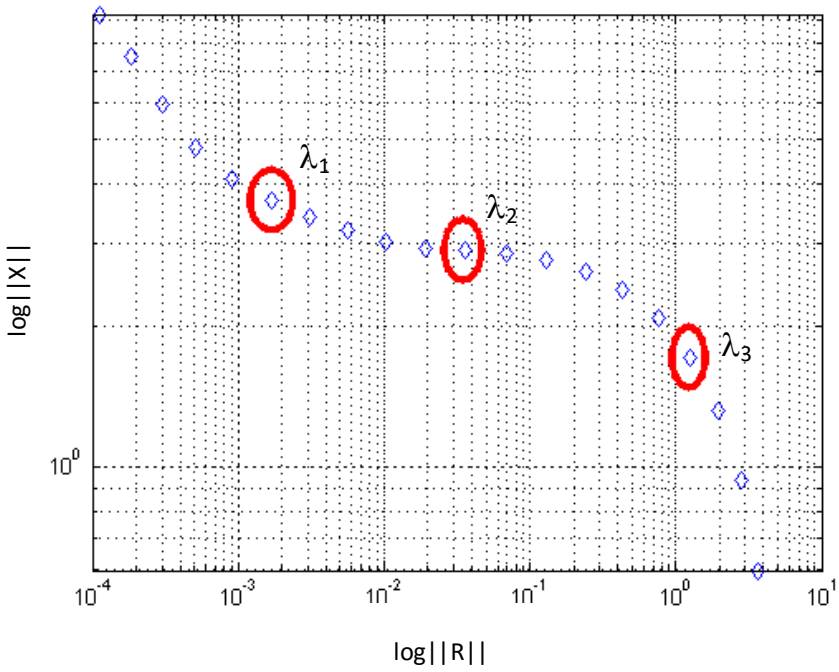

Figure 4.8. L-curve for the case represented in Figure 4.2 to decide on regularization parameter

is calculated using forward finite difference approximation as suggested in [34]. Jacobian size increases with number of nodes used to define the void fraction over TIM1, resulting in higher computational times. In order to save computational time, the void fraction is defined based on a coarser node distribution and size of unknown void fraction vector is reduced to 11×11 along x and y axis, respectively (total of 121 nodes). The coarser void fraction vector meets the requirements for sensitivity study as finer voids do not cause a remarkable change in Thermal Performance Test (Test-1) as shown in Figure 4.1. The Jacobian matrix calculation uses approximately 2000 seconds with Intel® i5 processor with 2.50 GHz frequency.

The estimated void fractions for the sensitivity case for simulated measurements (data with no error) and synthetic measurements (data with random error and uncertainty) are presented in Figures 4.9-4.11. Figure 4.10 represents the solution when the standard deviation of the random error introduced is σ while random error is 2σ for the solution shown in Figure 4.11.

In all cases, estimated void fraction values at several nodes are out of the range [0, 1] leading to unphysical solutions. In order to keep void fraction in physically possible limits, ad-

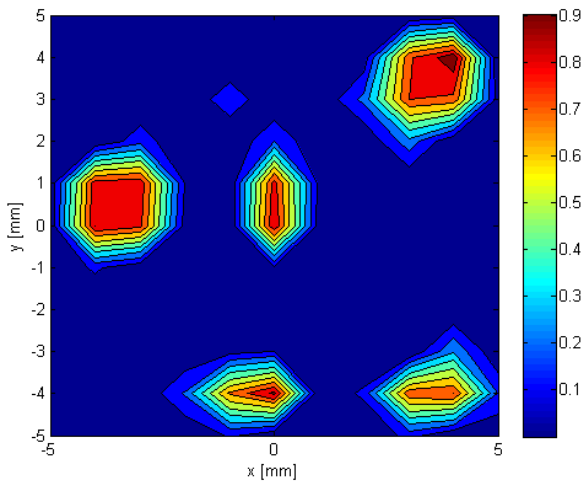

Figure 4.9. Ad-hoc filtered void fraction estimation for the case in Figure 4.2 for measurements with no random error

hoc filtering is applied by rounding void fraction values greater than 1 and smaller than 0 to 1 and 0, respectively. The average of absolute error in void fraction estimation for the case with simulated measurement is 0.052 while maximum absolute error is 0.38. The convergence criterion is satisfied after 8 iterations for simulated measurements with no error. Estimated void fractions in Figure 4.9 show that the location and value of the void fraction are both predicted accurately while void shapes are slightly different than those of the actual distribution presented in Figure 4.2.

Void fraction estimations for synthetic measurements with uncertainty and random error σ and 2σ are represented in Figures 4.10 and 4.11, respectively. For the cases with synthetic measurements with σ and 2σ including uncertainty, corresponding average absolute errors are 0.17 and 0.20 while maximum absolute errors are 0.76 and 1, respectively. Void fraction is estimated after just 3 iterations for the cases relying on synthetic measurements due to more relaxed convergence criterion. However, estimation accuracy decreases compared to inverse crime case shown in Figure 4.9, due to error introduction to measurement data. It can be observed that the voided regions spread to areas in between two neighboring voids. Some small voided regions can be observed at the edges, as well. Figures 4.10 and 4.11 indicate that as measurement error increases, estimation accuracy decreases. Additional voids are more

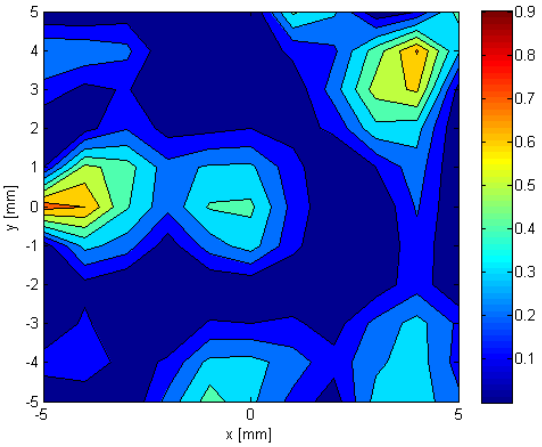

Figure 4.10. Ad-hoc filtered void fraction estimation for the case in Figure 4.2 for measurements with uncertainty and random measurement error σ

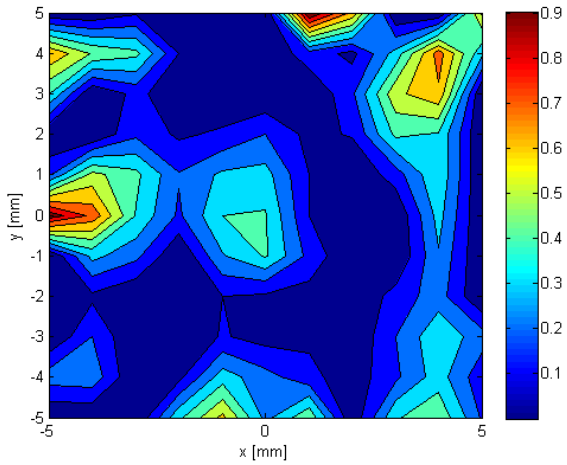

Figure 4.11. Ad-hoc filtered void fraction estimation for the case in Figure 4.2 for measurements with uncertainty and random measurement error 2σ

observable at the edges and voids spread over a larger area between two voids, i.e. voids 4 and 5 as labeled in Figure 4.2, with the increase in random measurement error.

For the simulations, results of which are presented so far, damping coefficient, λ, is altered by 0.1 at each iteration as shown in Figure 2.5. In an effort to improve estimation results, the effect of coefficient of alteration of damping coefficient at successive iterations is investigated. For this purpose, a parametric study is performed for the case shown in Figure 4.2

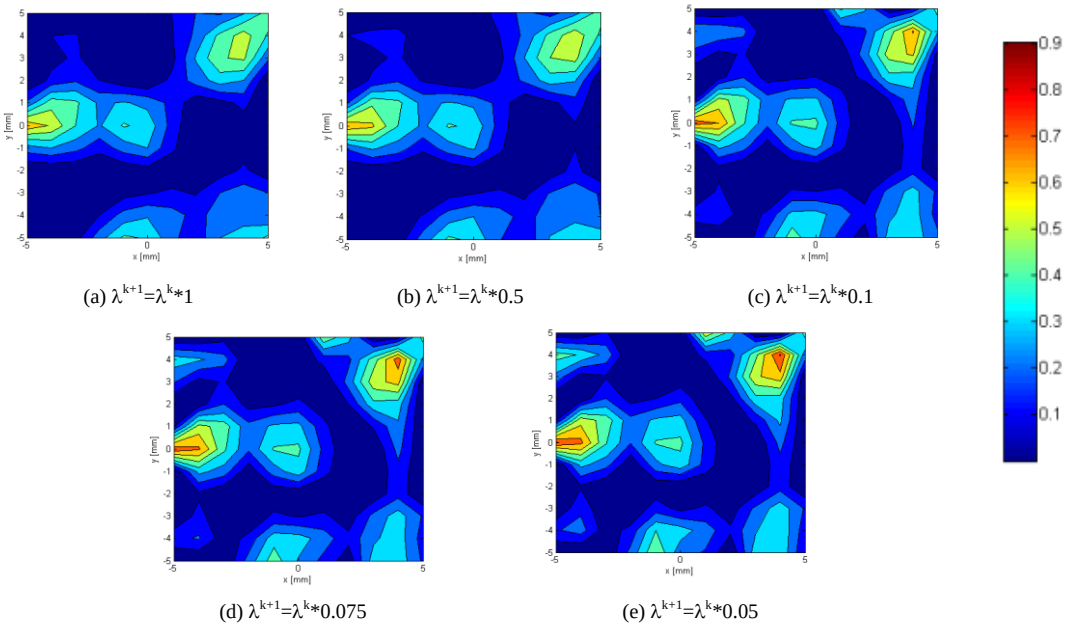

(a) $\lambda^{k+1}=\lambda^{k}*1$ (b) $\lambda^{k+1}=\lambda^{k}*0.5$ (c) $\lambda^{k+1}=\lambda^{k}*0.1$

(d) $\lambda^{k+1}=\lambda^{k}*0.075$ (e) $\lambda^{k+1}=\lambda^{k}*0.05$

Figure 4.12. Void fraction estimation for parametric study for alteration coefficient for λ at each iteration in LMA for the case in Figure 4.2 with uncertainty and random measurement error σ

by multiplying λ by a range of values between 1 and 0.05. In all cases, estimated void fraction values at several nodes are out of the range [0, 1] leading to unphysical solutions. In order to keep void fraction in physically possible limits, ad-hoc filtering is applied as for previously presented estimations. Estimation results are shown in Figure 4.12. It should be noted that as damping coefficient decreases, smearing of voids is more visible while estimations at voided locations are better. Considering Figure 4.12, it is concluded that [0.05-0.1] range is reasonable for alteration coefficient of λ at each iteration.

Similarly, in order to demonstrate the limits of the proposed method, optimum temperature data collection duration and time step is investigated. For this purpose, effect of total test time on void fraction estimations is compared first for 50 ms, 100 ms and 200 ms duration with 5 ms-time-intervals. The results are illustrated in Figure 4.13. Test duration of 50 ms results in smearing of voids as data time is not long enough to identify system behavior accurately. On the other hand, 200-ms-test does not converge and results do not represent system properties, which can be an expected outcome as thermal signal disappears for long

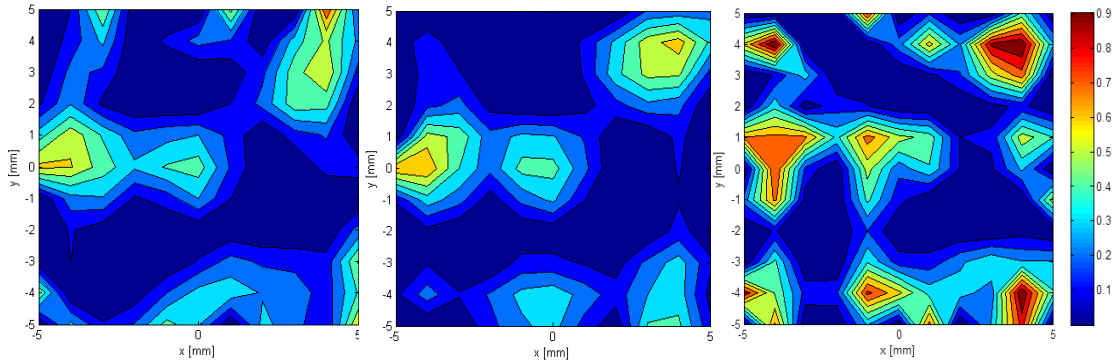

(a) t=0:5:50 ms (b) t=0:5:100 ms (c) t=0:5:200 ms

Figure 4.13. Ad-hoc filtered void fraction estimations for the case in Figure 4.2 for measurements with uncertainty and random measurement error σ to investigate optimum measurement duration

experiment durations. Therefore, 100 ms is selected as the optimum test duration for our specific problem.

For better void fraction estimations, optimum temperature data collection step is investigated as well. For this purpose, estimations are compared for the same duration (100 ms) with different time intervals ranging from 5 ms to 20 ms. Corresponding results can be seen in Figure 4.14. It is concluded that there is a trade-off between smearing of voids and estimation accuracy in regards to measurement interval. As time interval increases, voids are estimated with higher accuracy at the cost of smearing. Considering this, Δt=10 ms is chosen as optimum time interval for data collection for the test system studied here.

In an effort to reduce smearing of voids, “dimensional reduction” is applied to the estimated void fractions. Jones *et al.* [38] zooms in non-homogenous regions by increasing number of finite elements blocks there after solving ordinary regularization problem. In this study, we adopt a similar approach by performing additional iterations after obtaining approximations as shown in Figure 4.10. We perform “dimensional reduction” by decreasing Jacobian size. A new Jacobian matrix is calculated modifying ad-hoc filtered void fractions

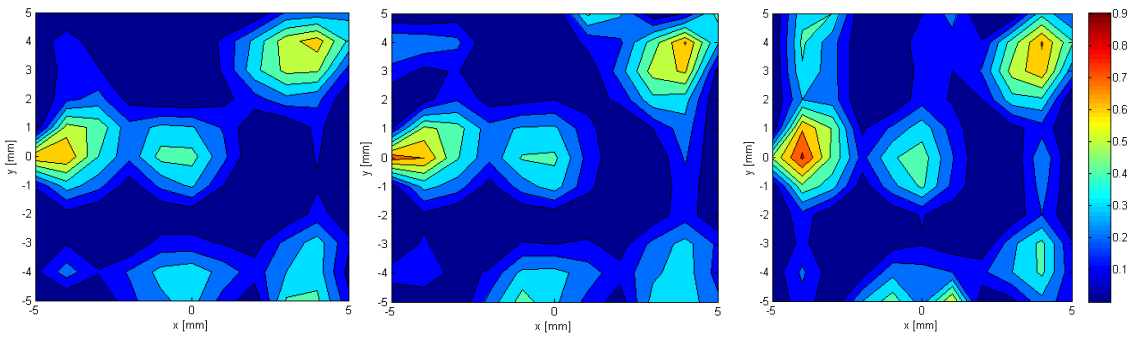

(a) t=0:5:100 ms (b) t=0:10:100 ms (c) t=0:20:100 ms

Figure 4.14. Ad-hoc filtered void fraction estimations for the case in Figure 4.2 for measurements with uncertainty and random measurement error σ to investigate optimum measurement time interval

only at the voided regions shown in Figure 4.10 while keeping void fraction values elsewhere constant. In order to keep Jacobian size smaller, number of grids at the voided regions is held constant in this study. For the synthetic measurement data with uncertainty and random measurement error σ, Jacobian size reduces to 2475×89. Iterations continue until previously defined stopping criteria $0.5N_sN_t\sigma^2$ is satisfied. The convergence is achieved just after 2 iterations for this case. Resulting estimation is shown in Figure 4.15. Although there is not a remarkable change in maximum absolute errors, average absolute error decreases to 0.13 for synthetic measurements with and random error σ. Smaller average absolute error implies that the method reduces smearing of voids, which can be observed from Figure 4.15.

In order to improve estimation accuracy, Levenberg-Marquardt algorithm presented in Figure 2.5 is modified so that after each iteration ad-hoc filtering is applied to the estimated void fractions and the points that reach physical bounds [0, 1] are removed from the Jacobian calculation, which is defined in Equation 2.20. This modification reduces Jacobian size at each iteration. Stopping criteria is also modified such that the algorithm continues iterations until the stopping criteria $F(\varphi^k) \leq 0.5N_sN_t\sigma^2$ or $F(\varphi^{k+1})-F(\varphi^k) \leq \varepsilon_2$ is satisfied. The algorithm stops when the difference between objective functions for successive iterations falls below $\varepsilon_2=10^{-5}$, even if the value of objective function is larger than $0.5N_sN_t\sigma^2$. For the synthetic measurement data

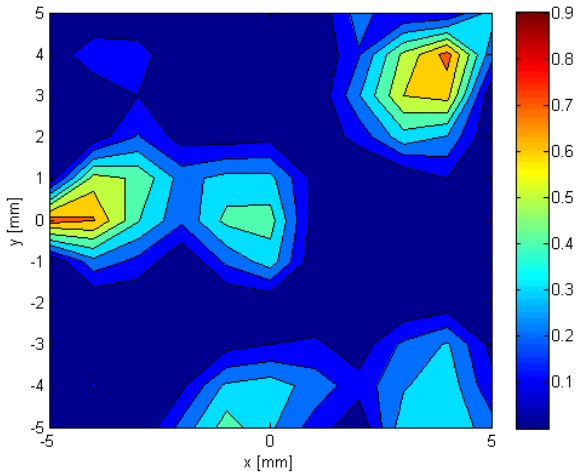

Figure 4.15. Ad-hoc filtered void fraction estimation for the case in Figure 4.2 for measurements with uncertainty and random measurement error σ using dimensional reduction

with uncertainty and random measurement error σ, Jacobian size at the final iteration reduces to 2475×44. The algorithm stops when $F(\boldsymbol{\varphi}^{k+1})-F(\boldsymbol{\varphi}^{k}) \leq \varepsilon_2$ is satisfied after 14 iterations for the case with synthetic measurement data with uncertainty and random measurement error σ. Estimated void fractions are presented in Figure 4.16. Average absolute error reduces to 0.11, implying that smearing reduces. Figure 4.16 shows that a phantom void is observed on top of void 1 as labeled in Figure 4.2. Despite the phantom void, this method provides better estimations with more accurate void fraction values at the voided regions, as illustrated in Figure 4.16.

Figures 4.10-4.11 and Figures 4.15 - 4.16 show that voids causing larger temperature rise in thermal performance test (Test-1) are estimated with better accuracy. In order to quantify estimation accuracy, average absolute errors for the estimations shown in Figure 4.10 and Figures 4.15-4.16 are calculated at the void coordinates. Corresponding temperature rise in Test-1 is illustrated in Figure 4.17 for synthetic measurements considering uncertainty and random measurement error σ. It is observed that estimation accuracy depends on effect of defect in thermal performance test (Test-1). The void fraction estimation gets better for voids

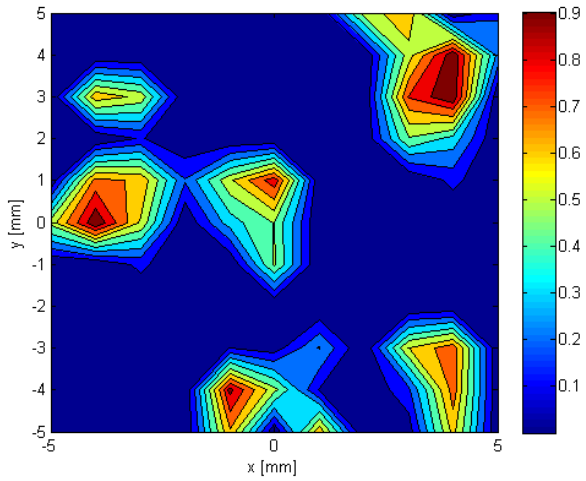

Figure 4.16. Ad-hoc filtered void fraction estimation for the case in Figure 4.2 for measurements with uncertainty and random measurement error σ, using ad-hoc filtering and dimensional reduction at each iteration

that are more effective on temperature rise in Test-1. Figure 4.17 also compares estimation accuracy for LMA, dimensional reduction adapted LMA and the modified LMA where ad-hoc filtering and dimensional reduction is applied at each iteration. Although error trend is similar for LMA and dimensional reduction adapted LMA, improvement in estimation accuracy for the largest void, i.e. void 5 as labeled in Figure 4.2, is remarkable. The final modification in LMA, which is performed by applying ad-hoc filtering at each iteration and excluding estimated void fractions that exceed physical bounds [0, 1] in Jacobian calculation, provides significantly higher accuracy compared to other two methods. Similarly, estimation accuracy for the largest void, i.e. void 5, that causes highest temperature rise in thermal performance test is estimated with the highest accuracy for this algorithm.

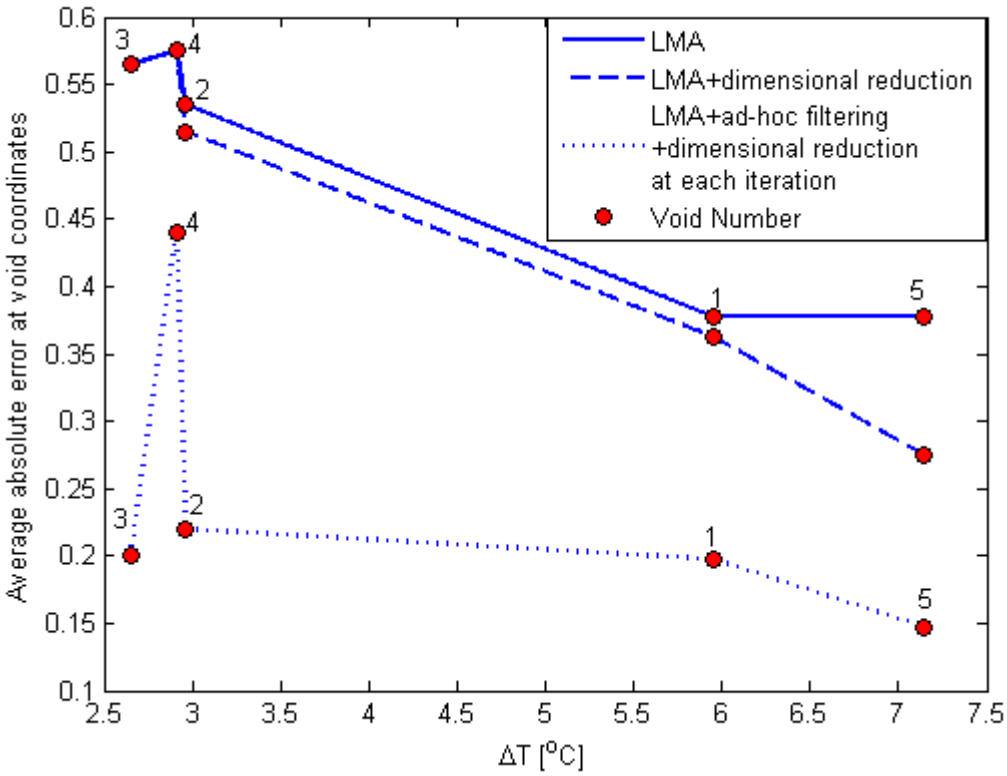

Figure 4.17. Effect of thermal performance test (Test-1) temperature rise on estimation results for measurements with uncertainty and random measurement error σ

5. CONCLUSION AND FUTURE WORK

The feasibility of thermal tomography as a quantitative means of defect detection in an electronic package, where spreading is effective due to different sized IHS and die, is investigated numerically. As defects within TIM1 layer have a prominent effect on thermal performance of the package, identification of defects within TIM1 is critical. Therefore, defects in TIM1 are considered in this study. Defects are modeled as voids, properties of which are considered to be identical to air properties. Use of thermal tomography for defect detection within TIM1 layer is demonstrated through simulated and synthetic measurements utilizing Levenberg-Marquardt algorithm (LMA) as image reconstruction technique.

Thermal performance test is applied first in order to identify whether TIM1 layer is defective. If a measurable temperature rise is observed as a result of thermal performance test, then thermal tomography is applied to characterize the defect. In order to show void size and location effect on thermal performance of the package and void fraction estimations obtained utilizing thermal tomography experiment, thermal performance test is applied one at a time to sample cases, each of which includes a void with a different size and at a different location. The result of this study is utilized to construct a sensitivity study, which is aimed to relate void size and location to estimation accuracy of thermal tomography experiment that is carried out numerically.

Measurement data for thermal tomography test is obtained solving the direct heat conduction equation using a FEM model created. This measurement data is utilized in resulting inverse tomography problem in order to estimate void fractions within TIM1 using LMA for simulated and synthetic measurement data. Before solving the inverse problem, ill-posed nature of the problem is identified using SVD. It was shown that the problem is highly ill-posed unless it is regularized. Afterwards, L-curve analysis is performed to make a decision about the initial regularization parameter. Optimum regularization parameter is chosen such that it keeps the balance between the solution and residual norm.

Estimation results indicate that estimation accuracy of void fractions decreases with the increase in measurement error. As measurement error increases, smearing of voids becomes

more observable. In an effort to improve estimations, optimum coefficient of multiplication for damping coefficient at each iteration is sought for. It was observed that as damping coefficient decreases, smearing of voids is more visible while estimations at voided locations are better. The range [0.05-0.1] is proposed as a reasonable range for alteration coefficient of λ at each iteration for 100 ms test duration.

In order to identify effect of total test duration on estimation results, thermal tomography test is conducted numerically for 50 ms, 100 ms and 200 ms durations with 5 ms time intervals. It was observed that 50-ms-test time is not as satisfactory as 100-ms-test as system information gathered in 50 ms was not sufficient to fully represent system behavior. Results indicate that convergence could not be achieved for 200-ms-test as thermal signal disappears with time due to lateral heat diffusion. Therefore, optimum duration for our thermal tomography test is selected as 100 ms. This case study indicates that gathering thermal signal that provides sufficient information about the system plays an important role in achieving better estimations with higher accuracy.

Effect of data collection time interval on estimation results is also studied by carrying out simulations for 100 ms test duration with 5 ms, 10 ms and 20 ms time intervals. Estimated void fractions show that there is a trade-off between smearing of voids and estimation accuracy considering measurement interval. As time interval increases, voids are estimated with higher accuracy at the cost of smearing. Therefore, Δt=10 ms is chosen as optimum time interval for data collection for the test system investigated.

In order to reduce smearing and increase estimation accuracy, a method similar to “zooming method” proposed by [39] is implemented in LMA using previous estimation results. We applied “dimensional reduction” for Jacobian matrix calculation. It was shown that dimensional reduction can filter smearing effect. For voids which are more effective on thermal performance of the system considering their size and location, improvement for the void fraction estimation is more observable. This method can be developed as a future work, by increasing grid numbers at the regions that are estimated as non-homogenous in LMA. Yet, this would increase size of the Jacobian matrix, resulting in higher computational times.

In an effort to obtain estimations with higher accuracy, LMA is modified by applying ad-hoc filtering at each iteration and removing void fractions that are equal to 0 or 1 from the Jacobian calculation. Although a phantom void was generated, this modification improved estimated void fractions remarkably.

In order to improve estimation accuracy, a statistical approach can be utilized to solve the inverse problem as suggested by [45-49]. This would come up with a longer computational time compared to deterministic methods. In order to overcome computational burden, a robust and efficient code for the direct problem of the solution, which provides measurement data, could be developed as a future work.

In this study, defects within TIM1 are considered as regions where air is trapped. However, other defects such as cracks can also be present between package layers. This study can be extended further in order to investigate cracks formed within package layers by formulating material properties as anisotropic. This study considers a uniform power map for thermal tomography experiment. As a future work, the method proposed can be tested for different thermal power maps. The method is useful for identifying defects causing larger temperature differences in thermal performance test. The validity of the method can be investigated by using the experimental measurement data.

REFERENCES

[1] Moore, G. E., "Cramming more components onto electric circuits", *Electronics Magazine*, Vol. 38, No. 8, pp.114-117, 1965.

[2] Gwinn, J., and R. Webb, "Performance and Testing of Thermal Interface Materials", *Microelectronics Journal*, Vol. 34, pp. 215-222, 2003.

[3] Pacheco, M., Z. Wang, L. Skoglund, Y. Liu, A. Medina, A. Raman, R. Dias, D. Goyal, and S. Ramanatham, "Advanced Fault Isolation and Failure Analysis Techniques for Future Package Technologies", *Intel Technology Journal*, Vol. 9, No. 4, pp. 337-352, 2005.

[4] Ertürk, H., "Evaluation of Image Reconstruction Algorithms for Non-Destructive Characterization of Thermal Interfaces", *International Journal of Thermal Sciences,*Vol. 50, No. 6, pp. 906-917, 2011.

[5] Gektin, V., "Thermal Management of Voids and Delaminations in TIMs", *IPACK*, San Francisco, 2005.

[6] Xu, Y., X. Wei, and G. Wang, "Temperature-Change-Based Thermal Tomography", *International Journal of Biomedical Imaging,*Vol. 2009, 2009.

[7] Pantong, N., A. Rhoden, S.H. Yang, S. Boetcher, H. Liu, and J. Su, "A globally convergent numerical method for coefficient inverse problems for thermal tomography", *Applicable Analysis*, Vol. 90, No. 10, pp. 1573–1594, 2011.

[8] Sun, J. G., D. O. Thompson, and D. E. Chimenti, "Quantitative Three-Dimensional Imaging By Thermal Tomography Method", *AIP Proceedings*, 2011.

[9] Swiderski, W., "The Characterization of Defects in Multi-Layered Composite Materials by Thermal Tomography Methods", *Acta Physica Polonica A*, Vol. 115, No. 4, pp. 800-804, 2009.

[10] Bakirov, V. F., and R. A. Kline, "Diffusion-Based Thermal Tomography", *Journal of Heat Transfer*, Vol. 127, No. 11, pp. 1276-1279, 2005.

[11] Cluff, K. D., “Electronic Packaging Technologies”,*Mechanical Engineering Handbook*, CRC Press LLC, 1999.

[12] Szendiuch,I., “Development in Electronic Packaging-Moving to 3D System Configuration”, *Radioengineering*, Vol. 20, No. 1, pp. 214-220, 2011.

[13] Staut V, E. A., “Characterization of Electronic Packaging Using Moire Interferometry”, M.S. Thesis, University of Illinous at Urbana-Champaign, 1997.

[14] Gao, S., “New Technologies for Lead-Free Flip Chip Assembly”, Ph.D. Thesis, University of London, 2005.

[15] Tummala, R., *Fundamentals of Microsystems Packaging*, McGraw-Hill, 2001.

[16] Mahajan, R. , C. P. Chiu, and G. Chyrysler, “Cooling a Microprocessor Chip”, *Proceedings of the IEEE*, Vol. 94, No. 8, pp. 1476-1486, 2006.

[17] Prasher, R., “Surface Chemistry and Characteristics Based Model for the Thermal Contact Resistance of Fluidic Interstitial Thermal Interface Materials”, *Journal of Heat Transfer*, Vol. 123, pp. 969-975, 2001.

[18] Chin, J. M., V. Narang, X. Zhao, M. Y. Tay, A. Phoa, V. Ravikumar, L. H. Ei, S. H. Lim, C. W. Teo, S. Zulkifli, M. C. Ong, and M. C. Tan, “Faut isolation in semiconductor product, process,physical an package failure analysis: Importance and overview”,*Microelectronics Reliability*, Vol. 51, pp. 1440-1448, 2011.

[19] Zhao, B., A. K. Asundi, and K. E. Oh, “Grid Method for Strain Measurement in Electronic Packaging Using Optical, Electronic, and Atomic Force Microscope”, *Proc. SPIE 3897, Advanced Photonic Sensors and Applications*, Vol. 3897, pp. 260-270, 1999.

[20] Maleki, H. R., A. A. Khatib, and F. Honarvar, “On the Nondestructive Evaluation of Composite Structures by Liquid-Crystal Thermography”, *17th World Conference on Nondestructive Testing*, Shanghai, China, 2008.

[21] Yang, Z. , W. Zhang, Y. Tian, Z. Li, and H. Zong, "Testing Application of Scanning Acoustic Microscope for Adhesive Characteristics of Explosive/Aluminum-Alloy Interface", *17th World Conference on Nondestructive Testing*, Shanghai, China, 2008.

[22] Partee, B., "The use of scanning acoustic microscope in electronic manufacturing applications", 2004, http://www.empf.org/empfasis/dec04/micro1204.htm, accessed at October 2015.

[23] Maur, F., "X-Ray Inspection For Electronic Packaging Latest Developments",*IEEE ICEPT*, Shanghai, China, 2003.

[24] Haque, A. S., "Characterization of Device Solder Interaction and Module Attachment for Power Electronics Modules", Ph.D. Thesis, Virginia Polytechnic Institute and State University, 1999.

[25] Azar, K., J. R. Benson, and V. P. Manno, "Liquid Crystal Imaging for Temperature Imaging of Electronic Devices", *Proceedings of 7th IEEE SEMI-THERM Symposium*, pp. 23-33, 1991.

[26] Gupta, A. , Y. Liu, N. Zamora, and T. Paddock, "Thermal Imaging For Detecting Thermal Interface Issues in Assembly and Reliability Stressing", *Thermal and Thermomechanical Proc.10th Intersoc. Conf. Phenom. Electron. Syst. ITHERM*, San Diego, 2006.

[27] Pacheco, M., and D. Goyal, "X-ray Computed Tomography for Non-Destructive Failure Analysis in Microelectronics Key Design Factors in X-Ray CT", *Reliability Physics Symposium*, 2010.

[28] Yamshchikov, Y., and K. Molchanov, "Electronic Components Nondestructive Testing: Comparison Between Acoustic Microscopy and X-Ray Analysis", *10th European Conference on Non-Destructive Testing*, Moscow, 2010.

[29] Burger, C., and J. Gryzagorides, "Transient Field Infrared Video Thermography as Procedure for Non-destructive Testing", *Proceedings Measurement Science Conference*, Palo Alto, 1983.

[30] Hadamard, J., *Lectures on Cauchy's Problem in Linear Partial Differential Equation*s, New Haven CT: Yale University Press, 1923.

[31] Soemers, M., "Numerical methods for the solution of a three-dimensional anisotropic inverse heat conduction problem", Ph.D. Thesis, RWTH Aachen University, 2008.

[32] Colaço, M. J. ,H. R. Orlande, and G. S. Dulikravich, "Inverse and Optimization Problems in Heat Transfer",*Journal of the Braz. Soc. of Mech. Sci. & Eng.,*Vol. 28, No. 1, 2006.

[33] Au, J. K., "An ab initio approach to the inverse-problem-based design of photonic bandgap devices", Ph.D. Thesis, California Institute of Technology, 2007.

[34] Özışık, M., and H. Orlande, *Inverse Heat Transfer: Fundamentals and Applications*, New York: Taylor and Francis, 2000.

[35] Ertürk, H., "Inverse Design and Control of Thermal Systems", Ph.D. Thesis, The University of Texas at Austin, 2002.

[36] Grysa, K., "Inverse Heat Conduction Problems, Heat Conduction-Basic Research, Prof. Vyacheslav Vikhrenko (Ed.)", 2011, http://www.intechopen.com/books/heat-conduction-basic-research/inverse-heat-conduction-problems, accessed at October 2015.

[37] Sawaf , B., and M. Özışık, "An inverse analysis to estimate linearly temperature dependent thermal conductivity components and heat capacity of an orthotropic medium", *International Journal of Heat and Mass Transfer*, Vol. 38, pp. 3005-3010, 1995.

[38] Jones, M., A. Tezuka, and Y. Yamada, "Thermal tomographic detection of inhomogenities", *Journal of Heat Transfer* ,Vol. 117, pp.969-975, 1995.

[39] Huang, H., and Y. Yan, "An inverse problem in simultaneously measuring temperature dependent thermal conductivity and heat capacity", *International Journal of Heat and Mass Transfer* ,Vol. 38, No.18,pp. 3433-3441,1995.

[40] Huang, H., and C. Chin, "A two-dimensional inverse problem in imaging thermal conductivity of a non-homogenous medium", *International Journal of Heat and Mass Transfer*, Vol. 43, pp. 4061-4071, 2000.

[41] Yang, C., "Determination of the temperature dependent thermophysical properties from temperature responses measured at medium's boundaries", *International Journal of Heat and Mass Transfer,*Vol. 43, No.7, pp. 1261-1270, 2000.

[42] Feuillet, V., Y. Jarny, and Y. Scudeller, "Estimation of thermal resistance distributions for die-attach testing in microelectronics", *Inverse Problems in Science and Engineering,* Vol. 15, No. 7, pp. 715-742, 2007.

[43] Toivanen, J., V. Kolehmainen, T. Tarvainen, H. Orlande, and J. Kaipio, "Simultaneous estimation of spatially distributed thermal conductivity, heat capacity and surface heat transfer coefficient", *International Journal of Heat and Mass Transfer,* Vol. 55, pp. 7958-7968, 2012.

[44] Toivanen, J., T. Tarvainen, J. Huttunen, T. Savolainen, H. Orlande, J. Kaipio, and V. Kolehmainen, "3D thermal tomography with experimental measurement data", *International Journal of Heat and Mass Transfer,* Vol. 78, pp. 1126-1134, 2014.

[45] Wang, J. , and N. Zabaras, "A Bayesian inference approach to the inverse heat conduction problem", *International Journal of Heat and Mass Transfer,* Vol. 47,No. 17-18, pp. 3927–3941, 2004.

[46] Gnanasekaran N., and C. Balaji, "A Bayesian approach for the simultaneous estimation of surface heat transfer coefficient and thermal conductivity from steady state experiments on fin", *International Journal of Heat and Mass Transfer,* Vol. 54, No.13-14, pp. 3060-3068, 2011.

[47] Kaipo, J., and C. Fox, "The Bayesian Framework for Inverse Problems in Heat Transfer", *Heat Transfer Engineering,* Vol. 32, No. 9, pp. 718–753, 2011.

[48] He, Y., "Rapid Thermal Conductivity Measurement With a Hot Disk Sensor Part 2. Characterization of thermal greases", *Thermochimica Acta,* Vol. 436, pp. 130-134, 2005.

[49] Machin G., R. Simpson, and M. Broussely, "Calibration And Validation Of Thermal Imagers", *9th International Conference on Quantitative InfraRed Thermography,* Krakow, Poland, 2008.

[50] Kurabayashi K., and K. Goodson, “Precision measurement and mapping of die-attach thermal resistance”, *IEEE Transactions on Components,Packaging,and Manufacturing Technology-Part A,* Vol. 21, pp. 506-514, 1998.

[51] Powell, R., C. Ho, and P. Liley, *Thermal Conductvity of Selected Materials*, Washington, DC: NSRD-NBS 8, 1966.

[52] Cheng, H., W. Chen, and H. Cheng, “Theoretical and experimental characterization of heat dissipation in a board level microelectronic component”, *Applied Thermal Engineering,* Vol. 28, pp. 575-588, 2008.

[53] Kays, W., M. Crawford, and B. Weigand, *Convective Heat and Mass Transfer*, Boston: McGrawHill, 2005.

[54] Özışık, M., *Heat Conduction*, New York: Wiley, 1980.

[55] Sweat, V. E., “Thermal properties of foods”, *Engineering Properties of Foods,* New York, Marcel Dekker.Inc, pp. 99-138, 1994.

[56] Ramos-Alvarado, B., D. Brown, X. Chen, B. Feng, and G. P. Peterson, “On the assessment of voids in the thermal interface material on the thermal performance of a silicon chip package”, *Microelectronics Reliability,* Vol.53, pp. 1987-1995, 2013.

[57] Orlande, H. , O. Fudym, D. Maillet, and R. M. Cotta, *Thermal Measurements and Inverse Techniques*, Boca Raton, FL: Taylor & Francis Group, 2011.

[58] Kline, S., and F. McClintock, “Describing uncertainities in single-sample experiments”, *Mechanical Engineering,* Vol. 75, pp. 3-8, 1953.

[59] Hansen, P. C., *Rank-Deficient and Discrete Ill-Posed Problems*, Philadelphia: SIAM, 1998.

[60] Crow, E. L., Davis, F. A., and M. W. Maxfield, *Statics Manual*, New York: Dover Publications Inc., 1960.

[61] Huang, C.H., and C.Y. Liu, “Thermal Tomography Problem in Estimating the Unknown Interfacial Surface”, *Journal of Thermophysics and Heat Transfer,* Vol. 25, No. 1, pp. 68-79, 2011.

[62] “Intel Xeon Processors”, http://www.intel.com/products/server/processor/xeon6000, accessed at June 2015.

[63] Huang, C.H., and C.Y. Liu, “Thermal Tomography Problem in Estimating the Unknown Interfacial Surface”, *Journal of Thermophysics and Heat Transfer,* Vol. 25, No.1, pp. 68-79, 2011.